An Experimental Study of Rim Formation in Single-Shot Femtosecond Laser Ablation of Borosilicate Glass

by

Priti Duggal, B.Tech.

Thesis

Presented to the Faculty of the Graduate School of
The University of Texas at Austin
in Partial Fulfillment
of the Requirements
for the Degree of

Master of Science in Engineering

The University of Texas at Austin
August 2006

An Experimental Study of Rim Formation in Single-Shot Femtosecond Laser Ablation of Borosilicate Glass

Approved by
Supervising Committee:

Adela Ben-Yakar

John R. Howell

Acknowledgments

My sincere thanks to my advisor Dr. Adela Ben-Yakar for showing trust in me and for introducing me to the exciting world of optics and lasers. Through numerous valuable discussions and arguments, she has helped me develop a scientific approach towards my work. I am ready to apply this attitude to my future projects and in other aspects of my life.

I would like to express gratitude towards my reader, Dr. Howell, who gave me very helpful feedback at such short notice.

My lab-mates have all positively contributed to my thesis in ways more than one. I especially thank Dan and Frederic for spending time to review the initial drafts of my writing.

Thanks to Navdeep for giving me a direction in life. I am excited about the future!

And, most importantly, I want to thank my parents. I am the person I am, because of you. Thank you.

11 August 2006

Abstract

An Experimental Study of Rim Formation in Single-Shot Femtosecond Laser Ablation of Borosilicate Glass

Priti Duggal, MSE
The University of Texas at Austin, 2006

Supervisor: Adela Ben-Yakar

Craters made on a dielectric surface by single femtosecond pulses often exhibit an elevated rim surrounding the crater. In case of machining with multiple pulses, the effect of the individual crater rims accumulates and shows up as surface roughness in the etched microfeature. Through experiments, we investigate the factors affecting the crater rim height and look at different methods for reducing the rim. The ultimate intention is to develop a femtosecond micromachining technique for etching smooth microfeatures on the surface of dielectric materials.

Experiments are carried out to study the relationship between the different ablation crater dimensions (diameter, depth and rim height). The crater diameter is a function of the laser fluence and the beam spot size. The fluence is varied from 5 J/cm^2 to about 30 J/cm^2 and the spot size is changed from 5 μm to 30 μm using different lenses in order to change the crater width. Additionally, moving the glass sample surface away from the focal plane of the focusing lens also alters the crater dimensions. Measurements show a clear inverse trend between the rim height, b, to crater depth, h, ratio and the square of the crater diameter, D, ie. $b/h \propto 1/D^x$, where x is presently unknown. As an example, an increase in crater diameter from 5 μm to 60 μm by varied means results in a decrease in the rim height/crater depth ratio from 0.6 to 0.05 or even lesser. Craters larger than 30 μm are typically rimless.

Also, we conclude from our experiments that for a given pulse energy and focusing conditions, the crater rims are observed to reduce in height by about 100 to 150 nm as the sample moves closer from the focal plane, towards the focusing lens.

Finally, we spatially reshape the Gaussian beam into a top-hat profile and show that the beam profile affects the rim height. Ablation with the top-hat beam profile provides relatively smaller rim heights and hence beam reshaping might be a beneficial technique for creating low rim craters with size smaller than 10 μm.

Table of Contents

List of Figures

List of Tables

1 Introduction

1.1 Introduction and Motivation

Femtosecond lasers offer a revolutionary tool for micromachining micron-scale three-dimensional structures either on the surface or in the bulk of any material [1-7]. They offer accuracy of less than one-tenth of a micron in applications requiring a high degree of precision such as tissue nanosurgery [8-12]. Being a direct write process, a femtosecond laser micromachining set-up can be used to etch complex geometries that can otherwise not be done by traditional lithographic techniques. Again, the short time duration of the laser pulses can be exploited to capture molecular level incidents by the laser [13-14].

All of this is possible because of the ultrashort duration of the pulses. Extremely high peak intensities can be achieved while keeping the average power low. The laser intensity is high enough to initiate non-linear absorption inside the target substrate, thus causing ablation. On the other hand, the low average power translates into minimal collateral damage. In other words, the damage is confined to a tight volume inside the material.

Since the high peak intensity laser pulses can be absorbed inside the material by a non-linear process, even transparent materials can be easily machined using a femtosecond laser.

Although there are multiple advantages to using femtosecond laser micromachining, the end result of multishot ablation is not very smooth. Cracks and other microfeatures are seen in case of surface ablation of dielectric materials like glass. These microfeatures can be explained by understanding the ablation process with single laser pulses [15]. A single shot ablation crater is typically surrounded by a 50-200 nm high rim. In case of multishot ablation, the rims of multiple craters overlap and diffractively interfere, resulting in microfeatures, and thus surface roughness.

The main purpose of this study is to experimentally study the rim formation process in single shot ablation craters, and to identify factors that influence the rim height, so that it can be reduced. Eliminating the crater rim should make the femtosecond laser ablation process a perfect tool for applications requiring precise and yet very smooth custom-designed channels, such as for lab-on-a-chip devices.

1.2 Theoretical Background

1.2.1 Femtosecond Ablation in Transparent Dielectrics

Glass is transparent because it is permeable to visible electromagnetic radiation or in other words, no linear absorption takes place inside it. When an ultrashort pulse laser (any wavelength) is incident on a dielectric like glass, the peak intensity of the beam is so high that it manages to non-linearly impart enough energy to the electrons to pull them from the valence to the conduction band, thus making them free electrons. These electrons, in turn, act as seed electrons and free yet more electrons by avalanche ionization. About 15-18 generations of avalanche ionization yields a sufficiently large electron plasma density to exceed macroscopic level ablation threshold.

At high laser energy, hot electrons and ions may explosively expand out of the focal volume into the surrounding material. This explosive expansion (ablation) leaves a void or a less dense central region surrounded by a denser halo. Densification of glass by femtosecond laser pulses can also occur. Which of these mechanism causes structural change depends on laser, focusing, and material parameters.

Nonlinear photoionization (direct excitation of the electron from the valence to the conduction band by the laser field) can happen in two ways depending on the laser intensity and frequency. In tunneling ionization, the electric field of the laser suppresses the Coulomb well that binds a valence electron to its parent atom. If the electric field is very strong, the Coulomb well can be suppressed enough that the

bound electron tunnels through the short barrier and becomes free, as shown schematically in the left-hand panel of Figure 1-1. This type of nonlinear ionization dominates for strong laser fields and low laser frequency.

At high laser frequencies (but still below that required for single photon absorption), an electron in the valence band absorbs enough photons so that the number of photons absorbed times the photon energy is equal to or greater than the band-gap of the material. This process, called Multiphoton Ionization, (MPI) is shown in the right-hand panel of Figure 1-1. More details can be found in [16]. The transition between tunneling ionization and MPI is decided by the Keldysh parameter [17].

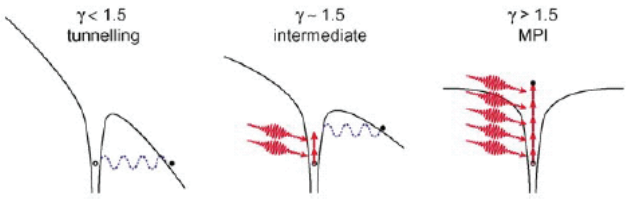

Figure 1-1: Schematic diagram of the photoionization of an electron in an atomic potential for different values of the Keldysh parameter. Tunneling Ionization is favored by strong laser field and low laser frequency. Multiphoton Ionization (MPI) is the dominant method of photoionization for high laser frequencies. [16]

The avalanche ionization process is schematically shown in the Figure 1-2. It involves free-carrier absorption followed by impact ionization [18]. An electron already in the conduction band linearly absorbs several laser photons sequentially. In order to conserve both energy and momentum, the electron must transfer momentum by absorbing or emitting a phonon or scattering off an impurity when it absorbs a laser photon. For electrons high in the conduction band, the deformation potential scattering time is approximately 1 fs, so frequent collisions make free carrier absorption efficient. After the sequential absorption of n photons, where n is the smallest number that satisfies the relation $n\hbar\omega \geq E_g$, the electron's energy exceeds the conduction band minimum by more than the band-gap energy E_g. The electron can then collisionally ionize another electron from the valence band, as illustrated in the right-hand panel of Figure 1-2. The result of the collisional

ionization is two electrons near the conduction band minimum, each of which can absorb energy through free carrier absorption and subsequently impact ionize additional valence band electrons.

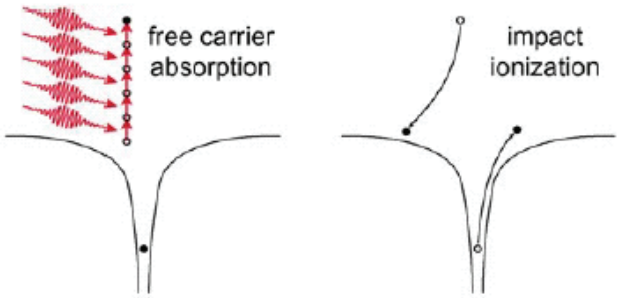

Figure 1-2: Avalanche Ionization. An initially free electron linearly absorbs several laser photons through free-carrier absorption, then impact ionizes another electron [16].

Interestingly, in the case of femtosecond laser pulses, photoionization by the leading edge of the laser pulse provides the seed electrons for avalanche ionization during the rest of the pulse [16]. Unlike the case with longer duration laser pulses, this self-seeded avalanche process does not require free electrons to be already present in the material in the form of surface/lattice defects or impurities, thus making the ablation process much more repeatable, and consistent from sample to sample. The femtosecond ablation rate, hence, depends on the material's intrinsic characteristics only (bandgap energy etc).

Energy is transferred from the free electrons to the heavy ions in the picoseconds time scale. The ions further transfer the energy to the lattice in the form of micrometer scale vibrations (exhibited as thermal effects on the macro-level) in the nanoseconds time scale. Thus the ablation can be executed with minimal thermal 'side-effects'; in other words, the ablation process is complete before the rest of the lattice can realize it! Ultimately, precise and controllable processing with minimal collateral thermal damage can be achieved compared to other laser machining approaches.

In comparison, in case of machining with nanosecond laser pulses, there is weak linear absorption in glass in the visible and the near infrared (NIR) range. The

pulse energy is thus absorbed in an extended volume in the glass, leading to thermal expansion inside, and hence increased internal stresses. This causes macro-cracking in the inherently brittle glass sample, limiting the precision of the machining process.

1.2.2 Accounting for Undesirable Effects

Non-linear effects and optical aberrations can cause the laser beam to get spatially and temporally distorted, thus affecting the ablated crater morphology and also introducing error into the measurement of factors such as the laser pulse energy and beam spot size at the sample surface. These factors need to be accounted for during the experiment. A brief discussion about the same is given below.

1.2.2.1 Non-Linear Propagation Effects – Self-focusing

Self-focusing is a result of the intensity dependence of the refractive index [19]

$$n = n_0 + n_2 I \qquad \textbf{...(1.1)}$$

where n is the total refractive index, n_0 is the ordinary linear refractive index coefficient and n_2 is the nonlinear refractive index coefficient. The spatial intensity profile in the laser pulse (usually Gaussian) leads to a spatial refractive index profile: because n_2 is positive in most materials, the refractive index becomes higher at the center of the beam compared to the wings. This variation in refractive index acts as a lens and focuses the beam.

As the power in the laser pulse is increased, self-focusing becomes stronger until, at some critical power, it balances diffraction and a filament is formed. If the peak power of the laser pulse exceeds this critical power for self-focusing then catastrophic collapse of the laser beam to a singularity is predicted [19]. The critical power, P_{cr}, is given by

$$P_{cr} = \frac{\pi (0.61)^2 \lambda^2}{8 n_0 n_2} \qquad \textbf{...(1.2)}$$

where λ is the laser wavelength. For borosilicate glass, n_0 = 1.52 and n_2 = 3.4 x10^{-16} cm^2/W [20] and thus P_{cr} = 1.8 MW.

In reality, as the laser beam self-focuses, the intensity rises and eventually becomes sufficient to nonlinearly ionize electrons in the free space. The electron gas contributes a negative refractive index change that cancels the positive refractive index change produced by the intensity-dependent index and prevents further self-focusing [21][22].

The laser intensity at the laser focus in the presence of weak self-focusing, I_{sf}, increases with increasing peak power, P, according to [16]

$$I_{sf} = \frac{I}{\left(1 - \frac{P}{P_{cr}}\right)} \qquad \textbf{...(1.3)}$$

where I is the laser intensity in the material in the absence of self-focusing.

While the threshold for optical breakdown and damage depends on the laser intensity, the threshold for self-focusing depends on peak power. If the laser pulse is tightly focused into the material using an external lens, the intensity for optical breakdown can be reached with powers that are below the critical power for self-focusing.

In transparent solids, the critical power is typically of the order of 1 MW (as calculated above) and the intensity threshold for bulk optical breakdown using a femtosecond laser pulse is about 10^{13} W/cm^2.

In the present analysis the energies used in the set-up are much higher than the critical energies, and hence the equations should account for self-focusing.

1.2.2.2 Optical Aberrations

Spherical aberrations occur when light rays at different heights from the optical axis are focused by the lens at slightly different distances along the axis. Since the maximum Numerical Aperture (*NA*) used in the experiments is 0.08, therefore spherical aberrations do not pose an issue for us [16].

Chromatic aberrations are caused when different wavelengths of the light incident on the focusing lens are not focused at exactly the same focal plane. The femtosecond laser used in the experiment has a wavelength bandwidth of about 9 nm only, hence this type of aberrations are not of concern in the experiment.

A coma aberration occurs due to rays entering the focusing lens at an angle, resulting in a circular object being imaged as a 'coma' in the imaging plane of the lens. This is minimized by ensuring that laser beam is normally incident on the lens (by looking at the back-reflection), and by using high quality optics.

1.2.3 Undesirable Damage during Femtosecond Ablation Process

Most of the incident laser energy goes into creating an electron plasma in the thin upper layer on the material. As the electron density in the plasma increases, it becomes more reflecting and more absorbing [23]. Due to the large electron density in that layer, it starts behaving like a metal; drastically decreasing the transmission, and hence limiting the ablation depth. The laser created surface plasma acts as a filter transmitting only the leading edge of the laser pulse. The transmitted energy is approximately fixed, nearly independent of the input pulse energy.

The rapid energy deposition in a thin surface layer creates an extremely large energy density, leading to intense shocks and a high pressure gradient in the zone. An immediate rapid rarefaction wave compensates for the shock. Both these effects contribute to increased stress in the material leading to microcracks. Most of the

energy ends up getting reflected from the surface, along with the high energy plasma.

Perry et al. [24] have shown that for high fluences (F>5-10 F_{th}, where threshold fluence, F_{th} ~ 2 J/cm^2 for fused silica), a large portion of the energy is reflected from the sample surface. For a laser fluence of ~ 10^{14} W/cm^2, they show that a few microseconds after irradiation, about 70% of the absorbed energy is used by the expanding plasma to move the ambient gas. 20% of the absorbed energy is lost as radiation to the environment, ultimately leaving less than about 3% of the incident laser energy as heat inside the material.

This thermal energy causes a thin layer of molten glass to be formed immediately beneath the ablation crater. The lifetime of the molten layer (including both the melting and resolidification processes) depends on how quickly the energy gets dissipated into the bulk. This depends on the material thermal properties (thermal conductivity, specific heat, density etc) [15].

Ben-Yakar et al [25] show that the melt flow in the borosilicate glass sample is caused principally by hydrodynamic forces due to the pressure gradient caused by the hot plasma sitting over the melt. The pressure gradient is extremely high at the edges of the ablated crater at the plasma/air interface. This results in some of the molten glass being ejected out of the crater over the edges of the crater. Rapid solidification results in the formation of a high rim surrounding the crater.

When craters are formed by multiple laser shots on the glass surface, the rims of the individual craters are seen to interact and influence each other [15]. This happens because the second laser pulse diffracts through the edges of the previously formed crater and creates a modulated light intensity at the bottom of the crater due to the interference of the diffracted light in the near field. This results in a ripple formed next to the crater rim. Similarly the third pulse gets diffracted again at the edges of the existing crater, leading to more microfeatures. The cumulative effect shows up as a macro-level surface roughness in the ablated structure.

Depending on the number of overlapping laser pulses at one spot on the substrate, the roughness can be exhibited as microfeatures, or as macrofeatures, or it can even be eliminated by self-annealing during the micromachining process [26][27].

Also, melting followed by a rapid cooling to the ambient temperature causes residual tensile stresses on the glass surface [28]. Ashkenasi et al. [29] have found that the hardness on the laser ablation crater edge is larger by at least a factor of six relative to non-illuminated areas when ablated with a 700 fs laser pulse. Therefore when an additional laser pulse is introduced near the area modified by the previous pulse, cracks will appear because of increased internal stresses.

1.2.3.1 In-Depth Discussion about the Crater Rim

As discussed above, the main force in play during the ablation process is due to the pressure gradient applied by the expanding plasma onto the molten material lying underneath. This plasma pressure forces the molten glass towards the periphery of the crater, thus directly influencing the free surface at the interface between the plasma and the melt. The molten layer at the edge of the crater faces an extremely high pressure gradient at the interface between the plasma and air. This pressure difference pushes the melt over the crater surface very rapidly. The pressure driven flow time τ_p thus determines the elevation of the melt above the surface, or in other words, this time duration decides the height of the rim. A shorter τ_p results in a higher elevated resolidified rim.

The characteristic time scale for this pressure-driven melt flow is [25]:

$$\tau_p \approx \frac{\mu L^2}{p_0 h_m^2} \qquad \textbf{...(1.4)}$$

where h_m is the average melt depth, p_0 is the average plasma pressure, μ is the viscosity and L is the crater width.

The melt depth is a function of the optical and thermal properties of the substrate, prominent factor being the threshold fluence for ablation for that material.

Based on heat transfer calculations, Ben-Yakar et al. [25] have estimated the melt depth to be of the order of about 1 μm and its lifetime τ_m to be of the order of about 1 μs.

With the estimated melt temperature exceeding 2500 K, the glass viscosity μ can be taken to be as small as 1 Pa.s [see Appendix B]. Typical crater width can be assumed to be 10 μm. The plasma pressure drops from a few millions of atmospheres at the start of ionization to about 10 atm after about 100 ns. Thus the average plasma pressure over the 100 ns time duration can be assumed to be ≈ 1000 atm. Hence, using equation 1.4, we estimate the pressure driven flow time, τ_p, to be of the order of about 100 ns.

Hence the pressure-driven flow time and the melt flow time are almost of the same order of magnitude. In case of τ_p being smaller than τ_m, the melt gets pushed out faster before it can resolidify, thus resulting in a rim.

Extending the above logic, since τ_m is almost constant for a given experimental set-up, therefore the rim height should have an inverse relationship with the time τ_p. Thus,

$$b \approx \frac{p_0 h_m^2}{\mu L^2} \qquad \textbf{...(1.5)}$$

where *b* is the rim height.

h_m is almost constant for a given material. An increase in the fluence implies an increase in the plasma pressure and temperature. This results in a melt with higher temperature, and hence lower viscosity. Both these factors contribute to decreasing the pressure-driven flow time, which in turn results in a higher rim. Hence rim height is directly proportional to the fluence. Since crater depth is a function of fluence, this translates into the direct proportionality between the rim height and the crater depth. Also, from equation 1.5, the rim height decreases as the crater width increases.

Therefore we expect to see a relationship between the rim height, crater width and the crater depth, such that the rim height is a function of crater depth/(crater width)^2, ie., $b \propto h/L^2$.

1.2.4 Possible Methods for Improving Machining Quality

In this project we try to design an experiment to improve the smoothness of channels made by multishot femtosecond laser ablation. Below we discuss some of the possible theoretical ways of doing this.

Use of minimum threshold fluence

Surface roughness seen in multishot ablation channels are because of the rims of individual craters formed by single pulses. Use of near threshold fluences during single spot ablation results in almost rimless craters. However the crater width and depth are extremely small and hence this method is not of much commercial use for obtaining smooth multishot ablation craters. Additionally the crater dimensions become more variable from shot-to-shot when we work in this fluence range.

Top-Hat beam profile

This method can also be used to reduce rim heights of single shot ablation craters, and has been explored in greater detail in the next chapter.

Pre- and post-machining annealing of glass

Stresses are developed in borosilicate glass when different parts of the crater made by a single femtosecond laser pulse cool down at different rates and can ultimately result in micro- or macro-cracking. These internal stresses can be relieved in the glass substrate by slowly heating it to the annealing point – the temperature at which the molecular arrangement is so altered within a reasonable period of time that the internal stresses disappear. After the internal stresses have been removed, the temperature is lowered very slowly so that all regions of the mass are at

practically uniform temperature during the cooling. This is to make sure that the mass shrinks uniformly and no strains develop.

It has been shown that annealing of glass sample, either before or after the ablation experiment, results in reduction of the height of bumps formed in glass by a laser [30]. The bump width remains unaffected. The reduction depends on the annealing conditions to a large extent. Also, the results are more drastic when the annealing is done after the ablation experiment.

Also, heating the glass substrate during the ablation experiment can ensure minimal cracking and hence better surface quality.

Machining conditions (inert gas stream, vacuum)

It is a well established fact that the use of an inert gas blowing at a steady velocity and pressure over the sample surface during the ablation experiment helps to blow away the debris created during the ablation resulting in cleaner ablation. Sun et al. [31] show that nonlinear self-focusing and plasma defocusing in an air or nitrogen environment can significantly distort the focused laser beam profile. However this distortion can be minimized by use of an inert gas shield, particularly helium, thus resulting in improved machining quality and efficiency.

Similar improvements in ablation craters have been made while performing the experiment inside a vacuum chamber.

1.3 Thesis Objectives

The ultimate objective of this project is to identify the factors that influence rim formation in craters created by single shot ablation of dielectric materials. The sample of choice is borosilicate glass.

Different techniques are tried to reduce the crater rim height, with special focus on reshaping the spatial intensity distribution of the beam from a Gaussian to a top-hat.

2 Laser Beam Spatial Profile

2.1 Gaussian Beam Theory

The subject of Gaussian beam propagation has been well researched [32]. However, a clear understanding of the terminology and the characteristics of the Gaussian beams is crucial in order to fully appreciate the experimental design and results. Hence, at the risk of repetition, some relevant discussion and definitions are given below for the reader's quick reference.

The Fourier transform of a Gaussian is a scaled Gaussian both in the near field and in the far field (unless intentionally reshaped); thus the beam profile remains Gaussian at every point along its path of propagation through the optical system. This makes it very convenient to work with lasers. Hence, most lasers are designed such that they resonate with a Gaussian distribution of the electric field.

The electric field distribution *E(r,z)* along the transverse (*r*) and axial (*z*) direction, measured in Volts/m is given by [32]:

$$E(r,z) = E_0 \frac{w_0}{w(z)} \exp\left(\frac{-r^2}{w^2(z)}\right) \exp\left(-ikz - ik\frac{r^2}{2R(z)} + i\zeta(z)\right) \quad \textbf{...(2.1)}$$

Here, E_0 is the peak electric field amplitude at the focal plane at the axis, w_0 = beam waist, $w(z)$ = beam radius at an axial location z, r is the radial co-ordinate, $R(z)$ = radius of curvature at z. $k = 2\pi/\lambda$ = wave number, for the design laser wavelength λ.

The time-averaged intensity distribution [W/m^2] is given by:

$$I(r,z) = \frac{|E(r,z)|^2}{2\eta} = I_0 \left(\frac{w_0}{w(z)}\right)^2 \exp\left(\frac{-2r^2}{w^2(z)}\right) \quad \textbf{...(2.2)}$$

As before, I_0 is the peak electric field intensity at the focal plane at the axis. η is the characteristic impedance of the medium in which the beam is propagating. For free space, $\eta = \eta_0 \approx 377\ \Omega$.

It is easier to measure the field intensity rather than the amplitude; hence the beam waist is normally calculated in terms of the field intensity. For the sake of consistency, the beam waist w_0 is defined in this thesis as the radial distance from the axis where the intensity falls to $1/e^2$ (or 0.135) of the peak intensity at the axis.

w(z) is defined as the beam waist, where the electric field amplitude E_0 and intensity I_0 drop to 1/e and $1/e^2$, respectively, at any axial location, *z*.

At the focal plane (z = 0), the transverse variation of electric field is hence given by:

$$E(r) = E_0 \exp(\frac{-r^2}{w_0^2}) \quad \textbf{...(2.3)}$$

And the electric field intensity is

$$I(r) = I_0 \exp(\frac{-2r^2}{w_0^2}) \quad \textbf{...(2.4)}$$

Hence, both *E(r)* and *I(r)* are Gaussian in shape.

As the Gaussian beam propagates, it experiences diffractive spreading beyond a certain distance, and hence the beam does not stay collimated over long distances. Thus, the beam radius and the radius of curvature change with axial distance.

The radius of curvature of the beam changes as

$$R(z) = z\left[1 + \left(\frac{\pi w_0^2}{\lambda z}\right)^2\right] \quad \textbf{...(2.5)}$$

and the radius of the beam changes as

$$w(z) = w_0\left[1+\left(\frac{\lambda z}{\pi w_0^2}\right)^2\right]^{1/2} \qquad \text{...(2.6)}$$

where λ is the wavelength of light, z is the distance propagated from the plane where the wavefront is flat, w_0 is the beam waist, $R(z)$ is the wavefront radius of curvature.

These trends are shown in the Figure 2-1 and Figure 2-2 below:

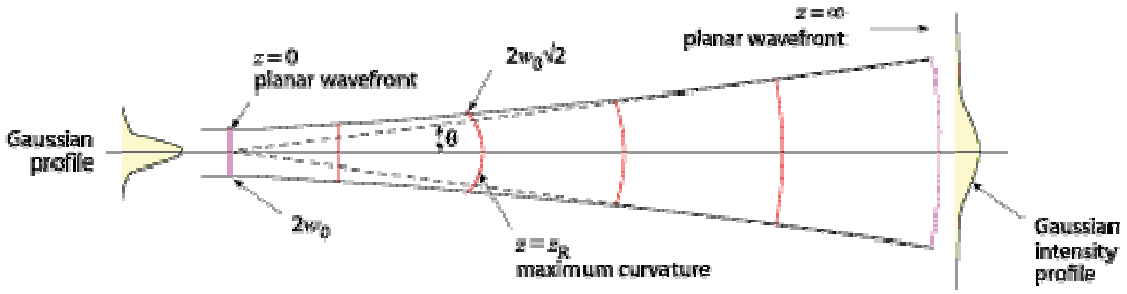

Figure 2-1: Change in beam profile and wavefront radius of curvature of Gaussian Profile with propagation distance [by courtesy of Melles Griot Inc.]

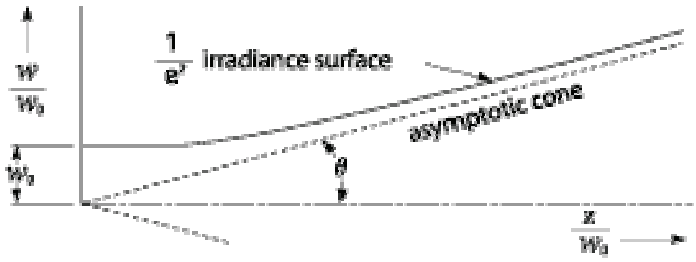

Figure 2-2: Growth in beam diameter as a function of distance from the Gaussian beam waist [by courtesy of Melles Griot Inc.]

The common parameter in eqns 2.5 and 2.6 is the Rayleigh range and is defined as the axial range over which the beam can be considered to be collimated. It is also called the confocal parameter. It is the axial distance from the focal plane where the beam cross-section becomes twice that at the focal plane, and can be considered to be the dividing line between the near-field and the mid-field range. Mathematically,

$$z_R = \frac{\pi w_0^2}{\lambda} \quad \text{...(2.7)}$$

R(z) is infinite at $z = 0$ (flat wavefront implies infinite radius of curvature, and hence $z = 0$ defines the beam waist location), passes through a minimum at $z = z_R$, and rises again toward infinity as z is further increased, asymptotically approaching the value of z itself.

At distances much beyond the Rayleigh range, the beam starts to diverge as a spherical wave from a point source located at the center of the waist. The half-angle divergence of the Gaussian TEM_{00} beam can be calculated as (Figure 2-1 and Figure 2-2):

$$\theta = \frac{w(z)}{z} = \frac{\lambda}{\pi w_0} \quad \text{...(2.8)}$$

Also, beyond z_R, the beam radius increases linearly along the axial direction, as

$$w(z) \cong \frac{\lambda z}{\pi w_0} \quad \text{...(2.9)}$$

The radius of curvature starts increasing linearly beyond the Rayleigh range:

$$R(z) = z\left[1 + \left(\frac{z_R}{z}\right)^2\right] \cong z \text{ ; } z \gg z_R \quad \text{...(2.10)}$$

All these equations are true on both sides of the focal plane.

2.1.1 M^2 Beam Propagation Factor

The fundamental TEM_{00} Gaussian mode of the laser beam ensures the smallest cross-section and the smallest divergence in the near field of the beam. Hence for applications requiring the laser beam to be focused to a small spot, the TEM_{00} mode is the ideal mode for the spatial beam profile. However, in the real world, this is almost impossible to achieve for a femtosecond laser beam. The higher the laser power, and the more complex the excitation mechanism for lasing to happen, the higher the deviation from a pure Gaussian profile. Truncation of the beam by any limiting apertures in the laser cavity also introduces fringes around the

main beam, thus affecting the beam profile. Presence of unnecessary harmonic modes in the beam profile causes the laser parameters to be unpredictable and unstable with time, and hence need to be accounted for in calculations.

Since a multimode combination of beams can have a nearly perfect Gaussian shape, calculations based on the Gaussian fit can be misleading. Instead, the M^2 (M-squared) beam propagation factor defined by Siegman [33] outlines a way of characterizing a laser, such that the exact focused spot size can be predicted for a given input beam width and lens focal length. Taking this one step further, the irradiance at a focused spot, the Rayleigh range and the far-field divergence of the beam can be calculated using the M^2 factor.

For a pure Gaussian beam [34],

$\theta = w_0/z_R = w_0/(\pi w_0^2/\lambda) = \lambda/\pi w_0 = 2\lambda/\pi d_0$

where d_0 and θ are the beam waist width and half divergence angle for an ideal Gaussian beam, z_R is the Rayleigh range, w_0 is the beam waist radius, and λ is the wavelength.

This gives:

$$d_0\theta = \frac{2\lambda}{\pi} \qquad \textbf{...(2.11)}$$

Real beams have a diameter-divergence product higher than the fundamental limit by a factor of M^2.

Thus, for real laser beams,

$$D_0\Theta = M^2\left(\frac{4\lambda}{\pi}\right) \qquad \textbf{...(2.12)}$$

where D_0 and Θ are the actual beam waist width and half divergence angle.

An interesting (though not typical) case is that of an 'embedded Gaussian beam' (shown in Figure 2-3). In this case, the real beam is everywhere larger than the ideal beam by *M*, thus forcing the divergence to be larger by a factor of *M*, thus

$$D_0\Theta = (Md_0)(M\theta) \qquad \text{(embedded Gaussian beam)}$$

Since divergence is calculated as $\theta = 2w_0/z_R$, therefore
$z_R = 2w_0/\theta = d_0/\theta = D_0/\Theta$ for an embedded Gaussian beam, i.e., Rayleigh range is the same for an embedded Gaussian beam.

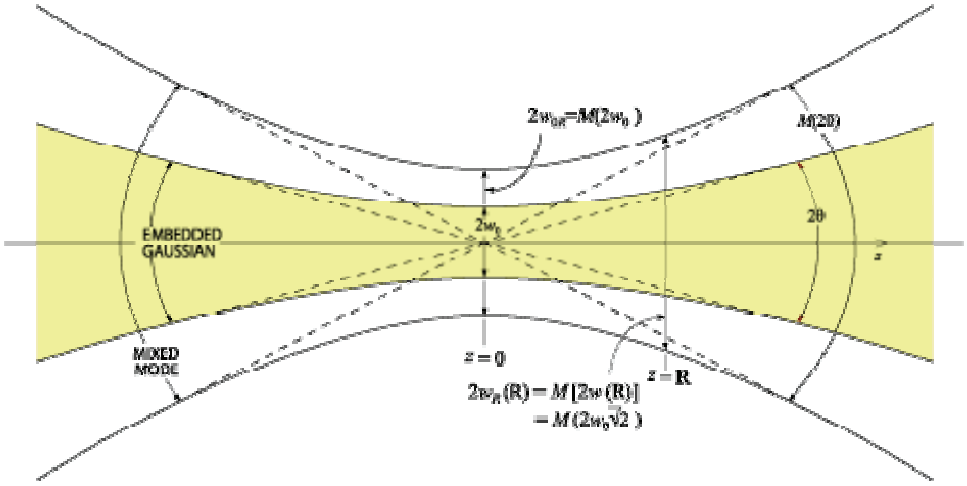

Figure 2-3: Embedded Gaussian beam. This case occurs quite infrequently. [by courtesy of Melles Griot]

Note that for usual cases, the M^2 factor can affect the beam waist size and/or the divergence, in any ratio.

Hence equations 2.5 and 2.6 get modified giving the radius and wavefront curvature of a real Gaussian beam with the following equations:

$$R_R(z) = z\left[1+\left(\frac{\pi w_{0R}^2}{M^2\lambda z}\right)^2\right]$$

$$w_R(z) = w_{0R}\left[1+\left(\frac{M^2\lambda z}{\pi w_{0R}^2}\right)^2\right]^{1/2} \qquad \text{...(2.13)}$$

where w_{0R} is the beam waist size of the real beam, $w_R(z)$ and $R_R(z)$ are the beam radius and wavefront curvature of the real laser beam at distance z from the beam waist, respectively.

2.1.1.1 Measuring M^2 factor

M^2 value is measured for the laser pulses of the femtosecond amplifier using the procedure outlined in the Appendix A.

The beam propagation factor is measured to be different along the x- and y- axes:
$M_x^2 = 1.8 \pm 0.04$
$M_y^2 = 1.2 \pm 0.07$

The difference between M_x^2 and M_y^2 is because the beam is slightly elliptical and it focuses at slightly different distances from the focusing lens along the two transverse axes.

2.2 Reshaping the Gaussian Beam Profile into Top-Hat

2.2.1 Introduction

The main intent of the project is to find methods of reducing surface roughness observed in micromachining with femtosecond lasers. As discussed earlier, this roughness seems to be the result of the rims seen to surround single-shot ablation craters. Reshaping the laser beam can offer a possible solution for this problem, as discussed below.

The most popular laser beam profile is the Gaussian intensity distribution, because it has the minimum divergence and stays collimated over a relatively long working range of a few hundred meters, depending on the beam diameter. This profile is excellent for alignment purposes. However, in case of machining with the Gaussian beam profile, the energy carried in the wings of the Gaussian distribution does not contribute effectively to the ablation process and is therefore wasted. This results in a lower part throughput and hence a higher production cost per part. Also, Gaussian beams can result in poor edge quality because the spatial energy distribution contributes to a wider heat-affected-zone (HAZ) around the illuminated area. Poor edge quality with signs of melting and spatter is observed. This is undesirable in applications involving drilling, scribing, marking or annealing.

In the case of micromachining with femtosecond laser pulses, the increased HAZ because of the Gaussian beam profile would cause relatively more substrate material to be molten, hence increasing the rim heights of the craters and the splash around the crater formed by single shot ablation. Overall this would show up as increased surface roughness.

Theoretically, if the Gaussian beam is spatially reshaped such as the intensity gradient in the outside region of the focused laser beam profile is increased, making the edges of the profile much steeper, with a uniform intensity profile in the middle portion, this top-hat or flat top profile should give an ablation crater profile with characteristics similar to the beam profile: straighter side-walls, uniform bottom. (Figure 2-4) It is expected that the ablation rate of the material will exhibit a spatial profile which is a mirror image of the incident beam intensity profile, removing at higher rates at the edges than at the center, as compared to ablation with a Gaussian beam.

The sharper edges of the beam profile should result in a smaller heat-affected zone along the sides of the crater, and hence less associated collateral damage, melt and crater rim formation. As compared to the original Gaussian function, the top-hat behaves like an energy step function with either enough energy to cause ablation or none at all. A melt zone will still be created beneath the ablation depth of the crater.

But there will be a lesser melt on the sides of the crater, ultimately leading to a smaller elevated rim around the crater.

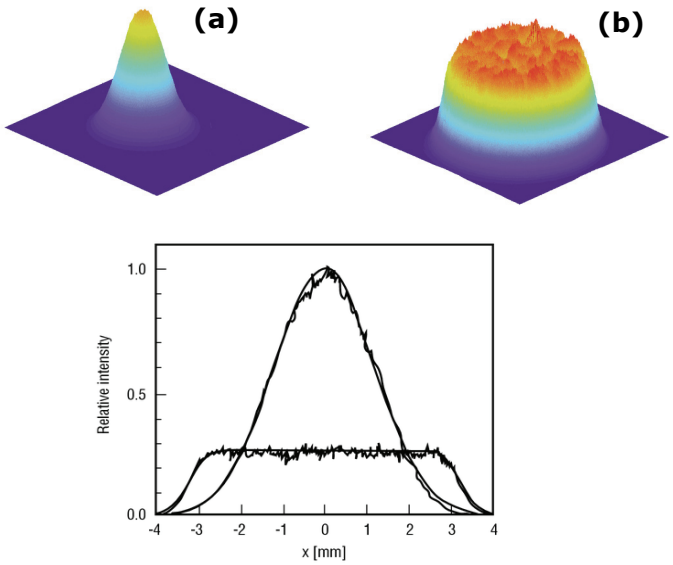

Figure 2-4: Comparison between (a) Gaussian and (b) top-hat laser beam profiles [Courtesy of Newport Corporation]

Also, if one uses multiple top-hat laser pulses, the walls of the crater so generated should be much smoother and more vertical as compared to the walls of the crater made by multiple Gaussian pulses.

Experiments done by Karnakis et al. [35] using a top-hat beam profile for machining polymers and silicon nitride (ceramic) with a Nd:YAG nanosecond pulse laser demonstrate improved edge quality, reduced roughness and wall roughness and a significant reduction in the energy density required for drilling microholes of high aspect ratio.

2.2.2 Theory behind Reshaping Gaussian into Top-Hat

A focusing lens behaves like a Fourier transform device; it performs a two-dimensional Fourier transform of the incident waveform at the speed of light. If an object (eg. transparency or aperture) is placed in the front focal plane of the lens and illuminated with coherent collimated light, the optical field at the back focal

plane of the lens will be the Fourier transform of the input object. This is a very well researched and well-understood phenomenon [36].

The project requires to create a uniform intensity profile at the focus of a lens. An inexpensive way of making a top-hat is by truncating the Gaussian beam with a small circular aperture. A Gaussian beam incident on a small diameter circular aperture behaves similar to a plane wave incident on a 'hard edge' circular aperture. When the 'plane wave' truncated by the aperture ('circ' function) is focused by a focusing lens, a Fourier transform of the aperture, an Airy disk pattern, is formed in the rear focal plane of the lens. This is in contrast to the focused image of the untruncated Gaussian beam, which is a scaled Gaussian, as discussed above.

If the distance between the aperture and the focusing lens is different from the focal length f, then a phase factor is introduced in the Fourier transform at the focal plane. This phase factor cannot be detected by the human eye or a beam profiler since both read the intensity pattern, and hence any information carried in the phase is thus lost. This phase factor can however be observed using interferometric methods. If the laser fluence is close to the threshold fluence for ablation, this additional phase factor might affect the ablation characteristics to some extent. In order to minimize this factor, the aperture is placed in the front focal plane of the lens. A typical experimental set-up is shown in Figure 2-5.

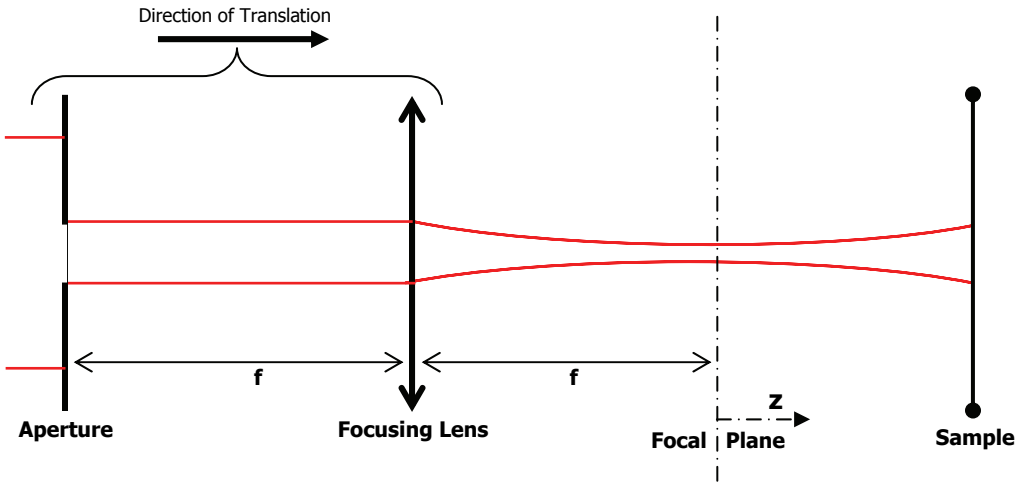

Figure 2-5: Schematic of Experimental Setup. A circular aperture is placed in the front focal plane of the achromatic focusing lens. Both the aperture and lens are translated together towards the glass sample surface.

The far field diffraction pattern of a source is observed in the focal plane of a focusing lens. This is because the wavefront is almost flat at the focal plane, which is the defining characteristic of the far-field regime (section 2.1). In contrast, outside the Rayleigh range of the focal plane, the curvature of the wavefront starts increasing linearly with distance from the focal plane, as per equation 2.10. The diffraction pattern transitions from far-field at the focal plane to mid-field beyond the Rayleigh range, and then finally near-field much further away from the focal plane.

In the far-field, the diffraction pattern is the exact Fourier transform of the object, albeit scaled in size. In the near field region, the diffraction pattern varies in both shape and size as we move away from the focal plane. Hence, when the object is a circularly truncated plane wave (top-hat) as in this experiment, the image resembles an Airy disk (Fourier transform of a top-hat) at the focal point of the lens. In the mid-field regime, the image is a combination of a top-hat and an Airy disk. The image becomes a perfect top-hat in the near-field region. This transition can be seen in Figure 2-6.

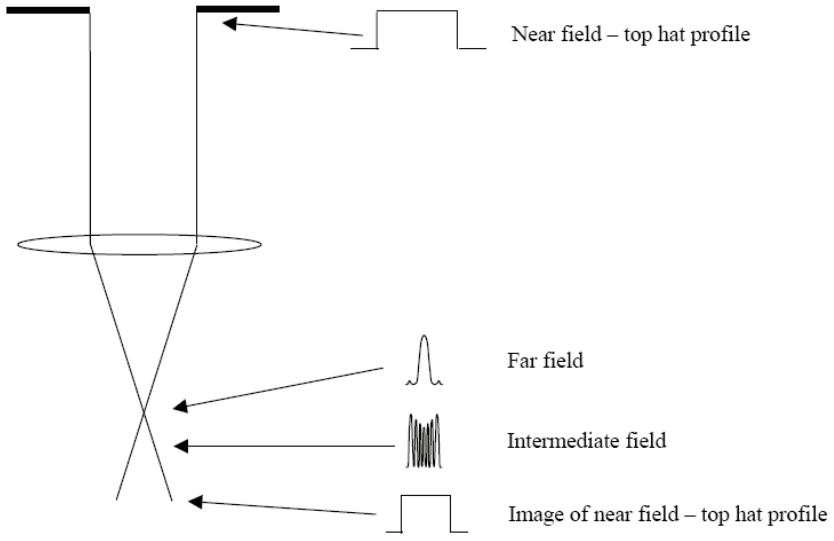

Figure 2-6: Schematic of typical beam profiles in the near field (laser output), far field (at the focus of a lens), and intermediate field [37]. The sharp edge aperture forms the top-hat wave-front which becomes the object for the focusing lens. Fraunhofer diffraction pattern is seen at the focal plane and Fresnel diffraction pattern is seen away from the focal plane.

In the real case, the sharp edges of the aperture introduce Fresnel rings into the beam profile (Figure 2-7). However, since the energy variation is about 10% and the walls are very sharp and straight (instead of the usual Gaussian profile) this should serve as a good top-hat for our purpose. Also, the diffraction ripples get smoothened out with distance, and hence better results are expected as the target moves away from the focal plane in either direction. Ideally, a soft edge aperture such as one with a Gaussian transmission function with 100% transmission at the center and decreasing transmission towards the edges should result in a Fourier transform without diffraction fringes.

Figure 2-7 therefore proves that using a truncating aperture provides a low cost solution for reshaping the laser beam, requiring minimal implementation effort.

A major disadvantage of using this method is that the aperture cuts off a lot of energy and hence this is a wasteful method, if implemented for commercial purposes for generating flat top beams. However it works successfully in providing a proof of concept for the current project.

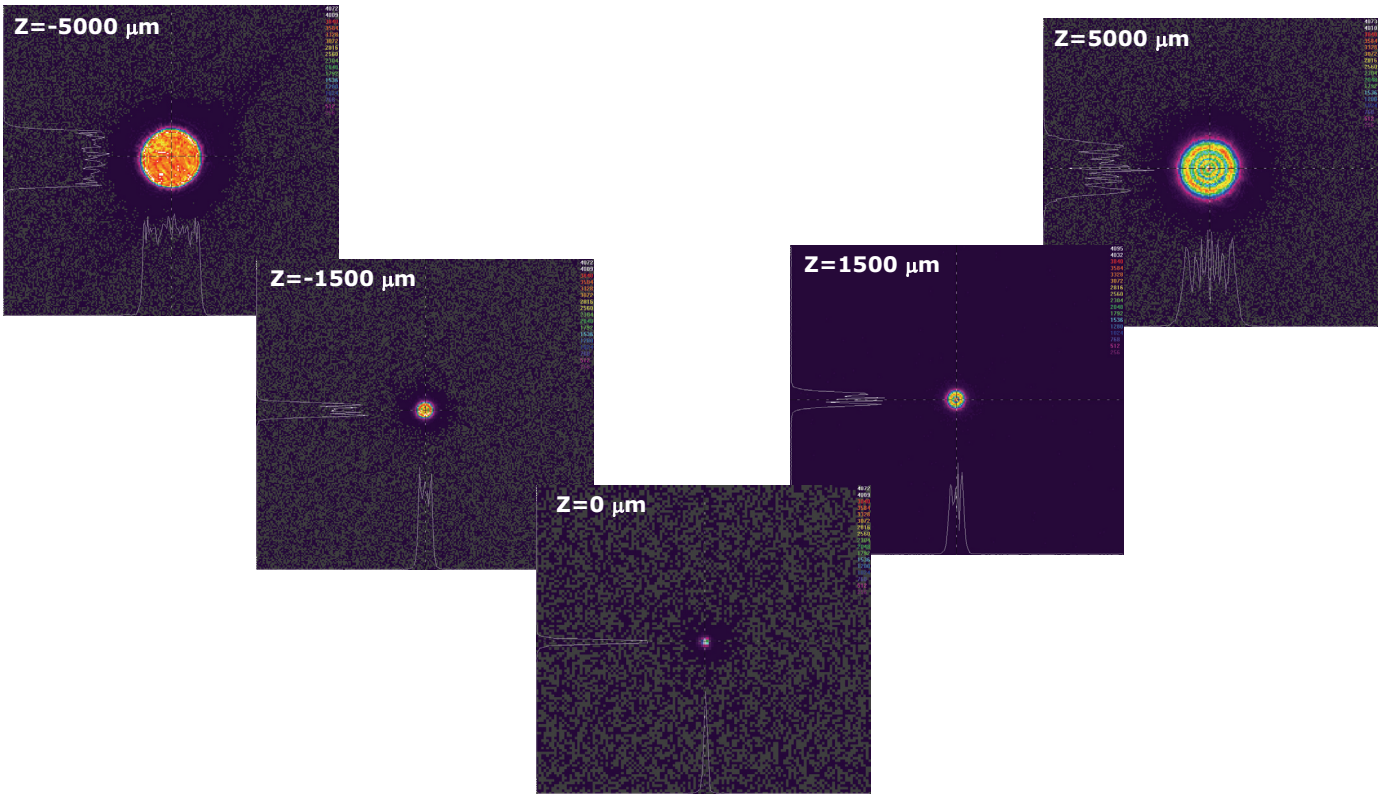

Figure 2-7: Beam profiler images of typical beam profiles in the near field (z= ±5000 μm), far field (z= ±0 μm), intermediate field (z= ±1500 μm). The images are made with a 10X *NA* 0.28 objective lens, with an aperture with diameter 3 mm in its front focal plane. The incident beam is expanded from 8 mm to 22 mm before the aperture. The beam profile represents an Airy disk at z = 0, and approaches a top-hat as we move away from the focal plane.

2.2.3 Alternative Methods for Creating a Top-Hat

The ideal method for generating a top-hat beam profile is to create a propagating Airy disk before the lens, such that the Fourier transform of the Airy profile (represented mathematically by a Bessel function) is a top-hat at the focal plane [38]. This can be done using a Diffractive Optics Element (DOE). For the desired focusing lens, we need to back-calculate the Fraunhofer transform pattern of the desired top-hat and then design a DOE element specific to that particular airy disk. Thus the set-up requires a customized DOE to be designed for every focusing lens. Also, the efficiency and effectiveness of a DOE also depends on the M^2 and the stability of the laser, which can be quite variable, depending on the optics. All factors put together, making a DOE can be an expensive proposition.

An alternative method of producing a top-hat is by using a pair of lenses to image a circular aperture. However, a real image is formed beyond the focal plane of the second lens. This is undesirable when working with a high power femtosecond laser since the focused beam causes non-linear ionization in the air, leading to the ionization of air at the focal plane, which can unpredictably change the beam profile.

The best method of creating a reliable top-hat beam profile is by modifying the laser cavity itself. For a given beam diameter, the lower the order of the mode, the lower the divergence. Consequently, for applications that involve focusing the beam to a small spot, or for propagating the beam over long distances, the laser should be constrained as best as possible to the TEM_{00} mode. However, if the main requirement is maximum power per unit volume, or if a constant intensity across the beam (a "top-hat" profile) is required, then a stable cavity that operates in a high-order mode will be appropriate.

3 Ablation with Gaussian Beam Profile

Surface ablation of borosilicate glass is carried out using high energy single femtosecond laser pulses with Gaussian energy distribution. The results are compared with those in existing literature, in order to gain experience in the experiments, and to calibrate our experimental set-up and procedure against known techniques. Once the ablation and imaging technique is well established and standardized, the effect of different ablation parameters (such as numerical aperture and pulse energy) on the rim height of the crater is studied.

3.1 Design of Experiment

The experimental set-up is quite simple and is shown in Figure 3-1. A combination of a half-wave plate and a cubic beam splitter are used for controlling the pulse energy (and hence, fluence). A focusing lens of focal length f is fixed on a z-axis 25 mm travel translation stage with a 0.5 μm step-size and placed in the path of the raw untruncated beam from the amplifier exit. The lens focuses the beam on a clean borosilicate glass sample (thickness 1.1 mm), which is fixed on an x-y-translation stage at approximately the rear focal plane of the lens. By checking the back reflection of the laser beam from the front surface of the sample, the sample is made normal to the direction of the incident laser beam.

Single shot ablation experiments are carried out with different laser pulse energies ranging from approximately 10 μJ to 1000 μJ. Also, the variation in crater morphology is studied while moving the target away from the focal plane of the lens.

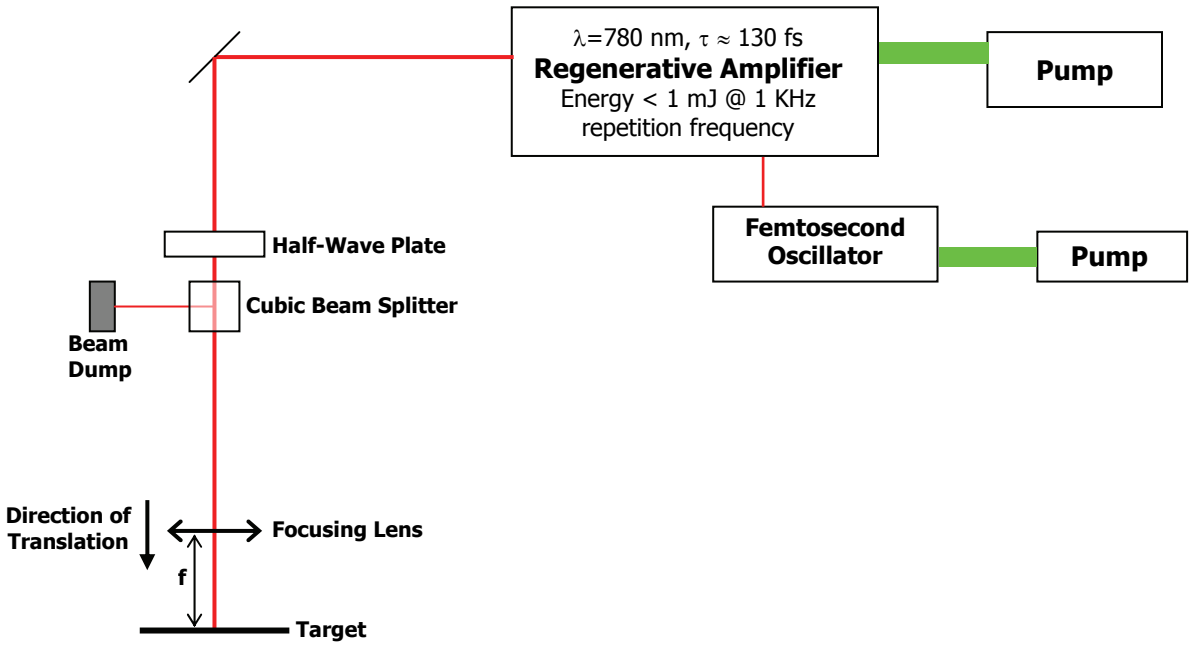

Figure 3-1: Top-View of Experimental Setup. The focusing lens is on a translation stage and is moved towards the glass sample in controlled step-sizes during the ablation experiment.

3.1.1 Setup Details

3.1.1.1 Laser system

The experiments are done with a kilohertz repetition rate Ti:Sapphire amplifier (Spitfire, Spectra Physics, Mountain View, CA) with the following specifications:

Pulse Energy (@ 1 KHz): ~ 1 mJ
Centerline wavelength: 780 nm
Pulse length at exit: ~130 fs
Beam diameter: 7.5 ± 0.5 mm (at $1/e^2$ of peak intensity), Gaussian spatial profile
Beam Propagation Factor, M^2: M^2_x = 1.8, M^2_y = 1.2
Polarization: linear, horizontal

Energy amplification is achieved in the amplifier using 'Chirped Pulse Amplification' (CPA); the technique involves temporally stretching the pulse,

amplifying it at reduced peak power, and then recompressing the amplified pulse near the exit, to close to its original pulse duration.

A single femtosecond duration pulse is isolated from the mode-locked pulse train from the femtosecond oscillator (Tsunami, Spectra Physics, Mountain View, CA), and becomes the 'seed pulse' for the amplifier. If this pulse is directly amplified, it can develop enough energy to destroy the gain medium through non-linear processes like self-focusing inside the crystal. To avoid this catastrophe, the CPA technique is used, whereby a diffraction grating first temporally stretches out the seed pulse by slowing down the high frequency components of the femtosecond pulse. This method works especially well for ultrashort pulses, since the bandwidth is large for a small laser pulse width (for a Gaussian pulse, $\Delta\nu\Delta t > 0.441$, where $\Delta\nu$ is the bandwidth, and Δt is the pulse width). The positively chirped pulse is now introduced into the gain medium of the amplifier while the crystal is being simultaneously optically pumped by the 1 kHz repetition rate frequency doubled 532 nm Nd:YLF laser. Pockels cells with response times of a few nanoseconds serve to ensure multiple passes of the seed pulse through the amplifier Ti:Sapphire, thus amplifying the pulse by about 10 times with each pass. An optimum number of passes of the pulse through the crystal ensures maximum cavity gain, maximum pulse energy and minimum pulse-to-pulse energy fluctuation. This requires that the instant when the amplified seed pulse is ejected from the gain cavity by the Pockels cell be carefully monitored. Finally the amplified pulse is recompressed to the original pulse width through the exact reverse process using another diffraction grating (negative chirp).

3.1.1.2 Energy Measurement

Pulse energy is measured after the focusing lens (immediately before the target) using a high-resolution energy meter by reducing the repetition rate of the amplifier from 1 kHz to 10 Hz and averaging over 1000 points. Pulse-to-pulse fluctuation is measured to be about 0.5%. During the actual ablation experiment, the continuous lasing mode of the amplifier is disabled, and the Pockels cell allows only one pulse at a time to be amplified inside the cavity. This causes the temperature of

the Ti:Sapphire crystal to drop. Therefore, for accurate pulse energy measurement, the repetition rate is decreased to 10 Hz to create the same environment inside the cavity (low operating temperature) as during the actual experiment.

3.1.1.3 Borosilicate Glass Substrate

Majority of this study was carried out on borosilicate glass (1.1 mm thick samples from 'Precision Glass and Optics Ltd.'), also known as Borofloat™. Borosilicate glass is chemically inert, hydrophilic, optically 100% clear, and relatively inexpensive and is therefore a favorite with chemists and biologists. This justifies our choice of substrate for this experiment. The properties of borosilicate glass are listed in Appendix B. The glass sample is cleaned with 'optical grade' methanol in an ultrasonic bath before and after each ablation experiment, to get rid of any debris or dust.

3.2 Post Ablation Analysis

Following laser processing, the sample with the single shot ablation craters is first observed under a reflection optical microscope (20X, 50X, 100X magnification) to measure the crater diameters in order to estimate the focal plane. It is also used to look at the quality of the prepared sample, before SEM and AFM analyses.

The crater morphology (depth, rim, presence of debris etc) is studied in detail by scanning the sample under an Atomic Force Microscope (AFM) (Digital Instruments Dimension 3100 with Nanoscope IV controller) under ambient conditions. All AFM topographic images are collected in the tapping mode by use of a 10 nm tip radius Silicon cantilever (MikroMasch) with a typical resonant frequency of 315 kHz and typical force constant 14.0 N/m.
Some of the craters are also observed under a Scanning Electron Microscope (SEM) (model: Hitachi S-4500 Field Emission SEM) operating at about 20 kV accelerating

voltage. Secondary electron images are generated to obtain 2-D information on the crater size, shape, recast layer, and crack formation at various locations.

3.3 Experimental Procedure

Keeping the laser energy fixed, the focusing lens is translated towards the sample surface in small controlled step sizes (Figure 3-2), and five single shot ablation craters are made on the sample surface for each axial position, to ensure statistical consistency. The single shot craters are at least 200 microns apart from each other, to make sure there are no diffraction effects because of the craters being too close [15].

The focal plane is estimated by using a knife-edge technique (razor blade and a beam profiling CCD camera). The knife is later replaced by the clean borosilicate glass sample. Estimating this location with a card using the naked eye is difficult because ablation can start much before the focal plane in case of a long confocal range. Also, the CCD camera can be used for looking at the focal plane, but since the exact location of the CCD array chip in the camera is difficult to measure accurately, this method is not good for locating the focal plane. After the single shot ablation experiment, the crater widths can be measured and the trend of the ellipticity can be used to accurately pinpoint the focal plane (Figure 3-2). This is discussed in more detail in section 3.5.1.

All experiments are performed in air at atmospheric pressure.

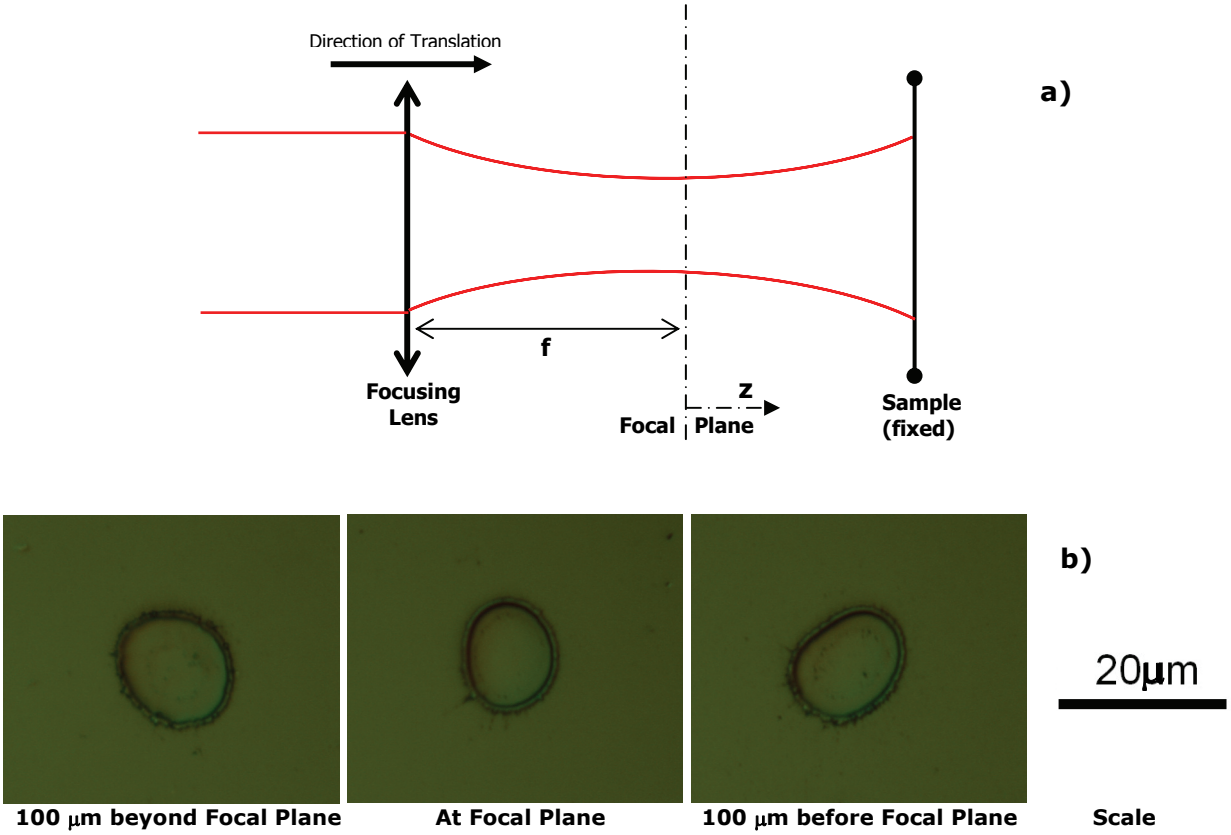

Figure 3-2: a) The focusing lens translates towards the target in all the experimental runs. Single shot ablation is carried out starting from the sample placed beyond the focal plane, till when it lies much before the focal plane. b) Sample optical images of single-shot ablation craters: E = 20 μJ, beam spot size = 6.2 μm, Gaussian beam profile, fluence ~ 16 J/cm^2

3.3.1 Data Available

Single shot ablation craters were made on the surface of borosilicate glass with the following experimental parameters:

f = 50 mm, *NA* = 0.08, E = 8,10,20,30,40,60,80 μJ
f = 100 mm, *NA* = 0.04, E = 32, 40, 80, 120 μJ
f = 250 mm, *NA* = 0.02, E = 103, 500, 1065 μJ

where f = focal length; *NA* = Numerical Aperture; E = pulse energy

3.4 Qualitative Analysis

The Numerical Aperture (*NA*) of an optical set-up characterizes the range of angles over which the system accepts or emits light. In the present context, if a laser beam of diameter $2w_0$ is incident on a lens of focal length f, the *NA* equals:

$$NA = \frac{2w_0}{2f} = \frac{w_0}{f} \qquad \textbf{...(3.1)}$$

Theoretical focused spot size, $w_1 = \frac{f\lambda}{\pi w_0} = \frac{\lambda}{\pi NA}$

Rayleigh range, $z_R = \frac{\pi w_1^2}{\lambda}$

Therefore, the higher the *NA*, the tighter the focusing and hence smaller the focused beam spot size. The Rayleigh range becomes short too.

Since the *NA* used in all experiments is less than 0.65, there is no concern for spherical aberration [16].

For high pulse energies, self-focusing needs to be accounted for in the experiments. As discussed in section 1.2.2.1, critical peak power for self-focusing to start is 1.8 MW. For a 200 fs pulse duration laser, the minimum average pulse energy required is $1.8 \times 10^6 \times 200 \times 10^{-15} = 3.6 \times 10^{-7}$ W = 0.36 μJ. This condition is fulfilled in all cases considered in this thesis. Hence the resulting laser intensity at the focus needs to be adjusted accordingly.

The self-focusing effect is especially prominent when the target lies beyond the focal plane, because the non-linear focusing of the laser beam in the air causes air-ionization and plasma breakdown, thus causing distortions in the beam profile. The non-elliptical crater shape and their non-uniform rims validate this reasoning. This can however be corrected by performing the experiments in a vacuum chamber at a pressure below 10^{-4} mbar [39].

Again, since all experimentation is done with single laser pulses, self-focusing should not be a problem for the cases with the glass surface either at or before the focal plane, unless very high fluences are used (> 20 J/cm^2).

1. Glass sample beyond the focal plane:

Careful perusal of Figure 3-3 shows the presence of an inner deeper elliptical region embedded inside the single shot ablation crater. Air dissociation starts to occur at an intensity of 4 x 10^{13} W/cm^2. Hence if the fluence is high enough, the air can get ionized at the focal plane, creating charged plasma that enhances the ablation of the glass surface in an uncontrolled manner. The distortion of the beam profile at the focal plane also results in non-elliptical craters.

Craters formed by tighter focusing exhibit uniform rims surrounding the craters and decreased debris. On the other hand, as the *NA* of the set-up decreases (implying looser focusing and larger crater sizes), the debris increases and the rim becomes relatively non-uniformly distributed around the periphery of the crater. This non-uniformity seems to follow a trend. Higher rims are seen on the sides of the ellipse across the major axis of the inner ellipse. This could be because along the high curvature boundary, the molten material finds lesser area to get redeposited in, leading to the higher rim.

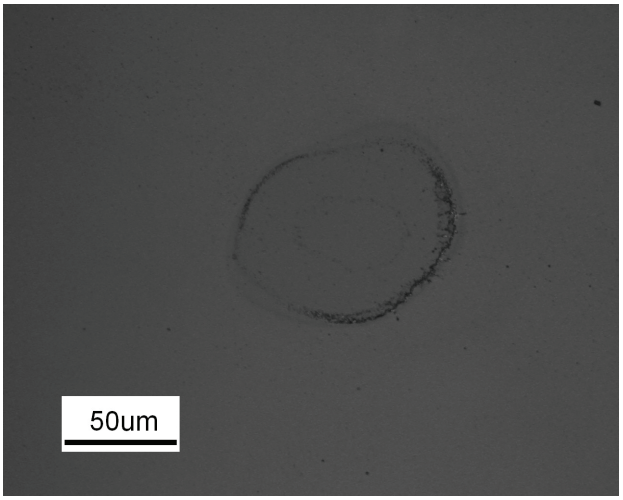

Figure 3-3: Optical image for single shot ablation crater made with f = 250 mm, E = 1000 μJ, with the glass sample beyond the focal plane of the lens. The non-uniform rim seems to be caused by the material ejected from the inner elliptical crater, and higher layer of material is deposited where there is lesser circumference available for deposition.

2. Glass sample at the focal plane:

There is a sharp, relatively high and uniformly distributed rim outside the crater. A typical example is shown in Figure 3-4.

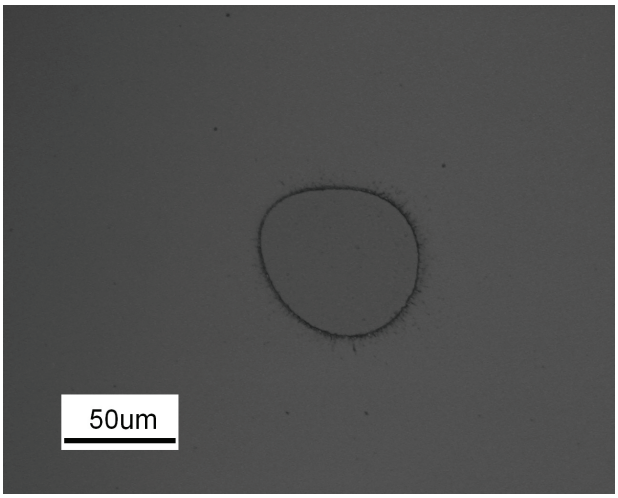

Figure 3-4: Optical images for single shot ablation craters made with f = 250 mm, E = 1000 μJ, with the glass sample at the focal plane of the lens. The rim is relatively high, and uniformly distributed around the crater boundary.

3. Glass sample before the focal plane:

All craters are elliptical in shape and are usually almost rimless (Figure 3-5). There seem to be two levels of ablation – the inner crater is deeper, and the so-called rim of the inner crater (formed of debris) is typically lower than the sample surface. There is a shallow 'moat' surrounding this inner crater and this might or might not have a rim slightly higher than the background surface. Since the focal plane is well inside the glass sample, or even behind it, there is just enough fluence available at the glass surface to cause minimal ablation. Most of the laser pulse is just enough to cause thermal melting of the glass. On cooling, this might cause the

material to compress and sink lower than the surface level. Or, as discussed by Schaffer et al [16], this could happen because of densification of glass by femtosecond pulses by breaking bonds in the material through multiphoton ionization.

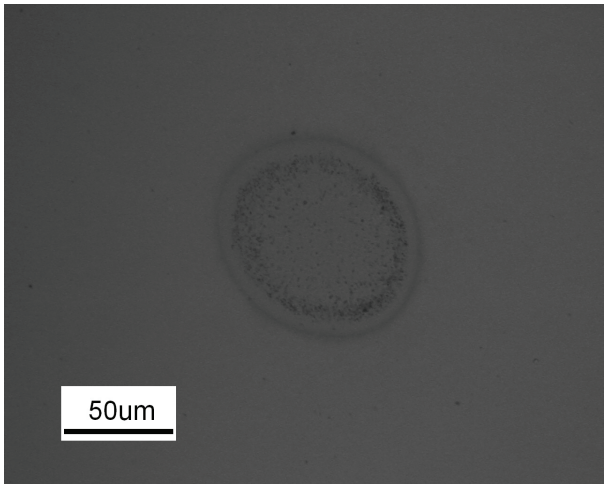

Figure 3-5: Optical images for single shot ablation craters made with f = 250 mm, E = 1000 μJ, with the glass sample before the focal plane of the lens. The inner rim is formed of debris and is uniform. These craters are typically rimless.

3.5 Quantitative Analysis

3.5.1 Crater Width, Beam Spot Size, Focal Plane Location

The single shot ablation craters made using the Gaussian beam profile are elliptical in cross-section, owing to the ellipticity of the laser beam. Optical images of the single shot ablation craters are used to measure the crater diameter along the horizontal direction, and also along the major and minor axes of the elliptical craters. Sample data is shown in the Figure 3-6 below:

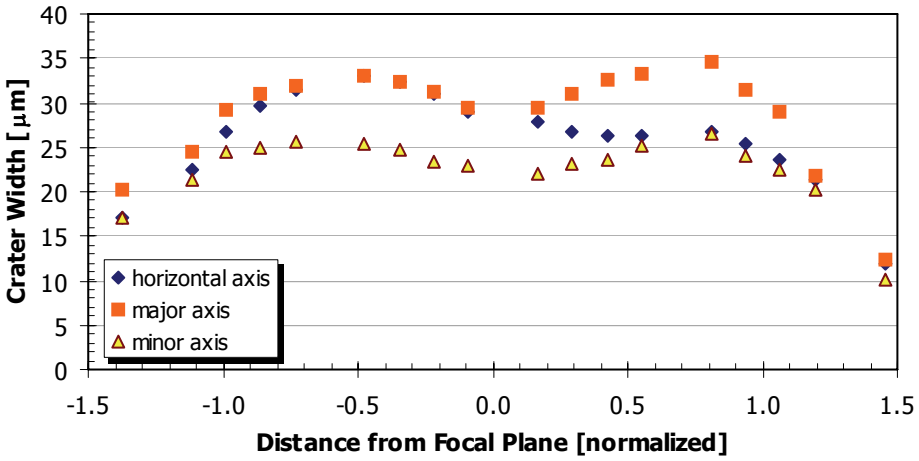

Figure 3-6: Variation in crater width as the lens moves closer to the glass surface. The x-axis is normalized by the Rayleigh range. There is a dip in the trend at the focal plane, as expected. Gaussian beam profile, f = 100 mm, E = 120 μJ. Crater width is measured along a) the axis of AFM scanning, b) major axis of elliptical crater, c) minor axis of elliptical crater. For later analysis, crater widths are measured along the major axis of the ellipse, to maintain consistency.

The trend is seen to be the same for the measurements along the major and minor axes respectively. For most of the analysis ahead, consistency is maintained by using the width measured along the major axis of the elliptical crater.

Increasing numbers on the x-axis of all the plots depicts the focusing lens moving closer to the glass sample. In other words, 'relative axial location' less than 'zero' implies that the glass sample is beyond the focal plane. 'z = 0' implies that the sample surface is exactly at the focal plane. Positive values indicate that the sample surface is closer to the lens than the focal distance. Refer to Figure 3-2 for experimental sketch.

At the focal plane, the crater width is expected to be the smallest. As we move away from the focal plane in either direction, the crater width should start increasing, gradually within the Rayleigh range and then steeply outside it. This is because the beam spot size in diverging while there is sufficient fluence to cause ablation.

The change in ellipticity (ratio of major diameter to minor diameter) of the elliptical craters as the lens moves towards the glass surface is graphed in Figure 3-7 below. Contrary to the expected trend, ellipticity is not the minimum at the focal plane. Since the beam propagation factor M^2 is different for the laser beam in the x- and y- directions, the beam focuses at slightly different distances from the lens in the two transverse directions, which causes the focal spot to be slightly elliptical too.

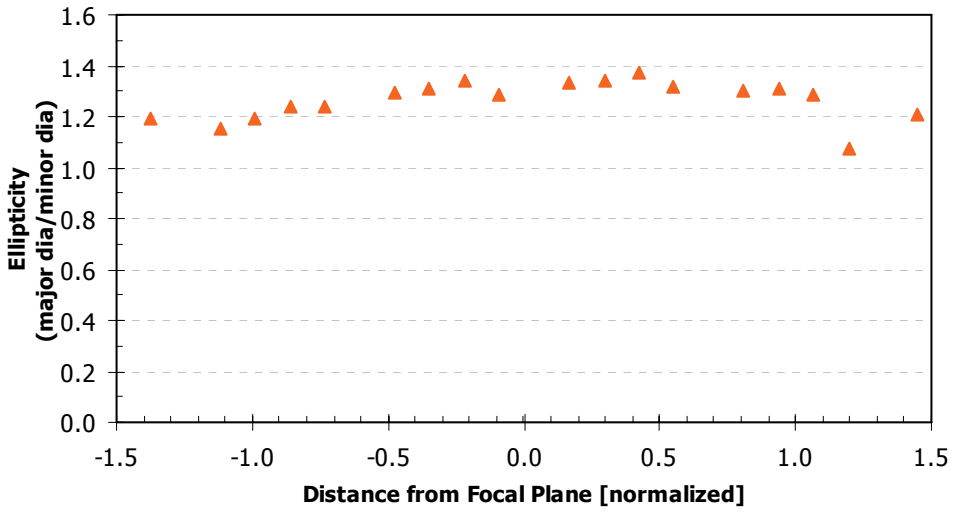

Figure 3-7: Typical case of variation in ellipticity of the elliptical single shot ablations craters as the lens moves closer to the glass sample. The x-axis is normalized by the Rayleigh range. No particular trend is observed.

Figure 3-8 below compares the variation in the crater width for different energies for a sample experimental set-up.

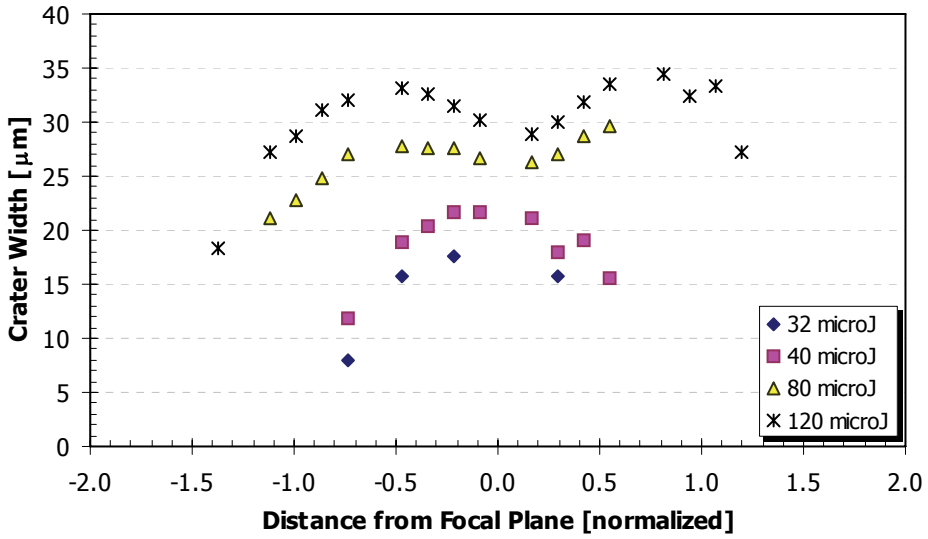

Figure 3-8: Variation of Crater Width as the Glass Sample moves towards the focusing lens, f = 100 mm (Experimental Data). beam spot size at focus = 13.9 μm. The x-axis is normalized by the Rayleigh range.

Given the average laser pulse energy E^{avg} and fluence F^{avg}, and the average threshold energy and fluence E_{th}^{avg} and F_{th}^{avg}, the crater diameter can be estimated as [39]:

$$D^2 = 2w_0^2 \ln\left(\frac{F_o^{avg}}{F_{th}^{N=1}}\right) = 2w_0^2 \ln\left(\frac{E}{E_{th}}\right) \quad \textbf{...(3.2)}$$

where w_0 is the beam spot size (radius) and D is the crater width at that location.

Focal length, f = 100 mm
Incoming beam radius, w_0 = 4 mm
Wavelength, λ = 780 nm
Ideal beam spot size (radius) at the focal plane, $w_1' = f\lambda/\pi w_0$ = 6.2 μm
Estimated beam propagation factor M^2 = 2
Expected beam spot size (radius) at the focal plane, w_1'' = 12.4 μm

Using an estimated beam spot size of 12.4 mm, we get the following crater width distribution with 'z' (Figure 3-9):

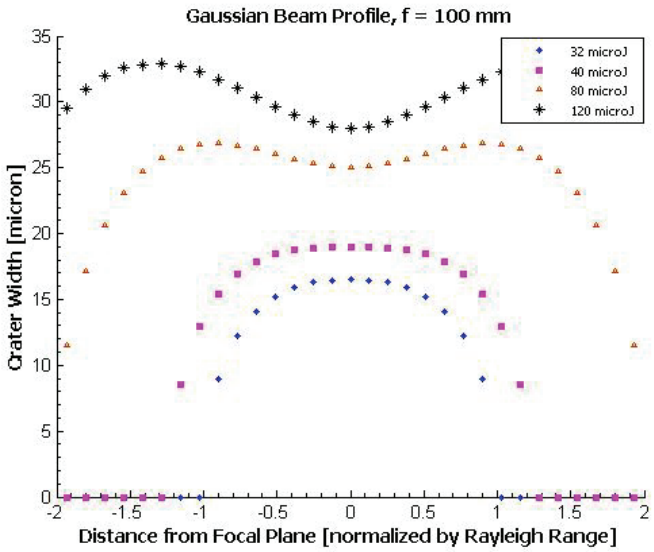

Figure 3-9: Expected variation in crater width with decreasing axial distance between the lens and the glass sample. This trend is seen to match with the experimental trend of Figure 3-6.

Hence, the experimentally obtained trends match with the simulations.

The focal plane is roughly estimated during the experiment by using a knife-edge and a beam profiler CCD. This value can be accurately estimated but since the knife-edge is replaced by the actual glass sample during the experiment, the focal plane location tends to shift by a few hundred microns. During the data analysis, the widths of the single shot ablation craters are measured using an optical microscope and plotted against z, the distance of the sample from the focal plane, as shown in Figure 3-8 above. The craters are expected to be the smallest at the focal plane, based on the MATLAB simulations. Based on this knowledge, the focal plane is then estimated. All the graphs in this thesis have been accordingly recalibrated.

The slope of the plot of the measured crater sizes D at different fluences (at a particular axial location) yields the beam spot size at that particular 'z', based on equation 3.2. Sample data is shown in Figure 3-10 for an arbitrary z location of 'z=1700'.

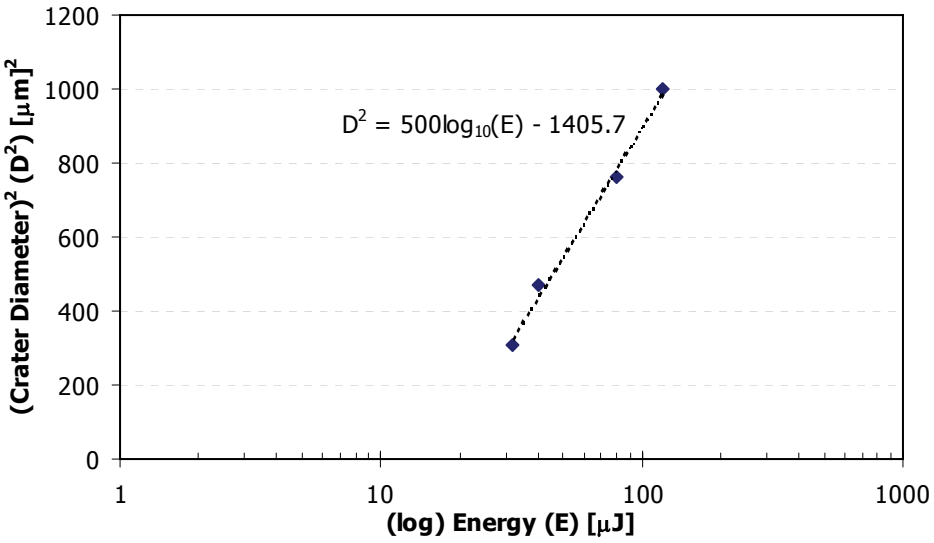

Figure 3-10: Variation in (crater diameter)^2 with energy for a given axial location of the glass surface with respect to the focusing lens (z/z_R = -0.2). The beam spot size at each 'z' can be calculating by finding the slope of each curve and using equation 3-2.

Air dissociation starts to occur at an electron intensity of 4 x 10^{13} W/cm^2. Assuming the femtosecond pulse duration to be about 200 fs by the time the laser pulse reaches the target, air ionization starts as soon as the fluence is more than 4 x 10^{13} W x 200 x 10^{-15} = 8 J/cm^2. Hence, fluences significantly higher than 8 J/cm^2 cause the data points to deviate from a linear trend [39].

The beam spot size so obtained for different 'z' values is then plotted against 'z' to show how the beam spot size varies as the focusing lens moves closer to the glass sample. This value is a function of the incoming beam size w_0, lens focal length f, laser wavelength λ, and is independent of the laser pulse energy. Figure 3-11 shows the case for f = 100 mm, incoming beam waist (radius) = 4 mm.

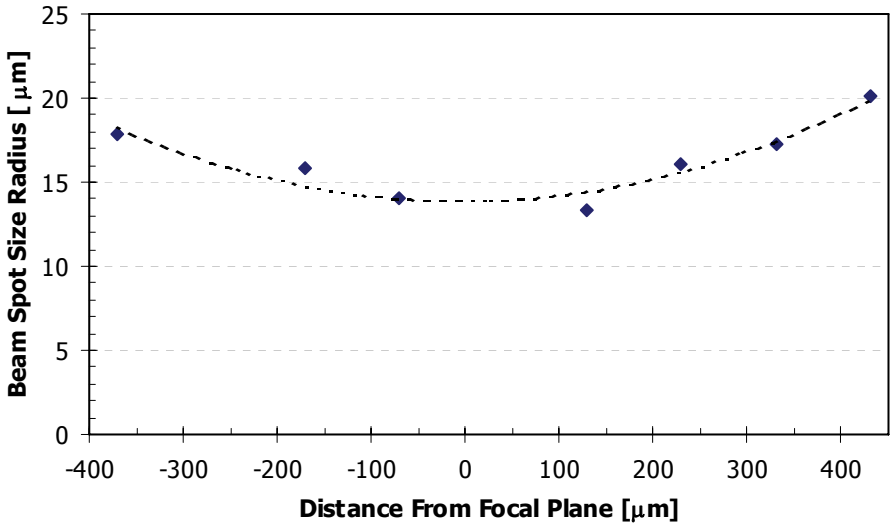

Figure 3-11: Variation in beam spot size with axial distance 'z' (distance between the glass surface and focusing lens). Calculated using analysis based on Figure 3-10. f = 100mm. Beam spot size at focal plane is approximately 13.9 μm.

From Figure 3-11, the actual beam spot size measured at the focal plane is w_1 = 13.9 μm. The ideal beam spot size (calculated above for f = 100 mm, w_0 = 4 mm) is 6.2 μm. Therefore calculated "Beam Propagation Factor" (M^2) is 13.9/6.2 = 2.2. This is close to the directly measured value of M^2 of 1.8 (section 2.1.1.1) and is acceptable within experimental error. Also, the Rayleigh range, z_R is 778 μm.

The Rayleigh range value is used to normalize the axial location of the glass sample surface w.r.t the focal plane of the focusing lens. This ensures that data obtained for experiments with different focused beam spot sizes and widely different energies can be compared with each other.

Equation 3.2 and Figure 3-10 are also used for estimating the single shot ablation threshold energy and hence fluence using the y-intercept value of the graph. $F_{th}^{N=1}$ is calculated for this experiment to be ranging between 2 to 2.5 J/cm^2.

3.5.2 Crater Depth

The crater ablation depth for a single-shot ablation crater can be estimated using the following equation, as long as the fluence is much higher than the threshold fluence.

$$h_a = \alpha_{eff}^{-1} \ln\left(\frac{F_0^{avg}}{F_{th}^{N>1}}\right) \quad \text{...(3.3)}$$

α_{eff}^{-1} is the effective optical penetration depth, and is assumed to be 240 nm when ablating in air [39]. $F_{th}^{N>1}$ is the multishot threshold fluence for the substrate calculated to be equal to 1.7 J/cm^2 (independent of atmospheric conditions).

Equation 3-3 is used for estimating the variation in the crater depth as the distance between the lens and the target varies, for the case of the lens with focal length f = 100 mm, and for different energies. The theoretical data is plotted using MATLAB in Figure 3-12 shown below. The crater is expected to be the deepest at the focal plane, where the fluence is the highest.

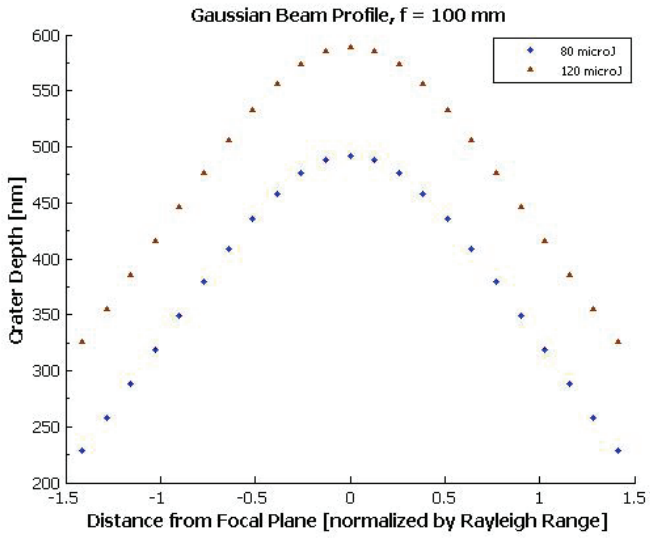

Figure 3-12: Calculated Crater Depth Variation with Distance from Focal Plane. The craters are deepest at the focal plane.

Experimental data for the crater depth obtained from the AFM scanned images is plotted in Figure 3-13 below:

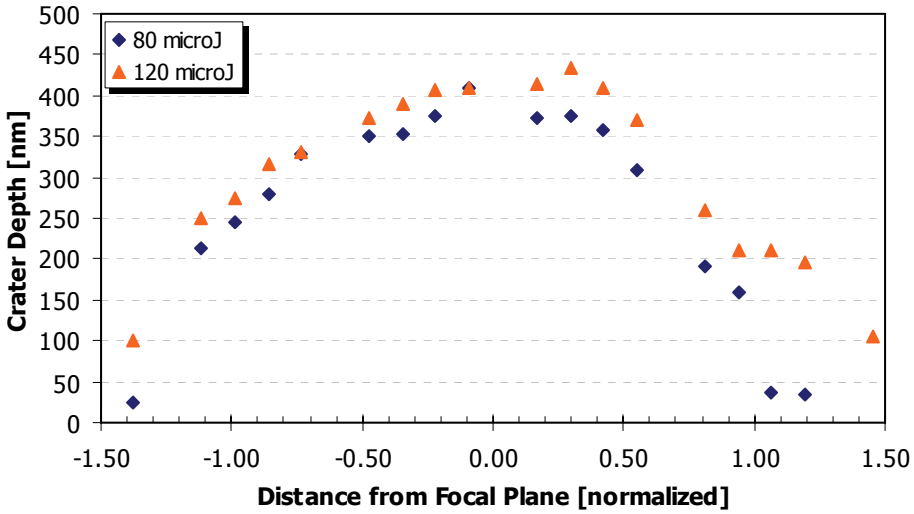

Figure 3-13: Experimental data for variation in crater depth as the lens moves closer to the glass surface. Beam profile: Gaussian, beam spot radius = 13.9 μm, f = 100 mm. The x-axis is normalized by the Rayleigh range.

The trend for the crater depth is as almost as expected from the MATLAB simulations. The actual measured crater depth values are however consistently about 150-200 nm smaller than the expected values. Most probably this can be explained by a discrepancy in the value of the optical penetration depth, which has been assumed to be 240 nm, based on literature survey [39].

It is interesting to note that the craters are the deepest when the distance of the glass sample surface is slightly less than the focal distance from the lens. When the focal point is within the glass sample, it should logically cause more material to be ablated, hence creating a deeper crater. However, since the sample has a finite thickness of 1100 μm, once the focal point moves outside the sample, much lesser material is ejected from the crater, causing the depth of the craters to decrease.

The crater depths for the 80 μJ craters are almost the same as expected. However, the depths for the higher 120 μJ craters are much lower. This could be

because once a critical free electron density has been created on the crater surface, any additional fluence is unable to create any more plasma, and cause additional damage. All the extra energy is simply reflected from the surface.

3.5.3 Crater Rim Height

The rim heights are measured from the AFM scanned images of the craters. Data for single shot ablation craters made with f = 100 mm, and 80 and 120 μJ pulse energies is plotted in the Figure 3-14 below.

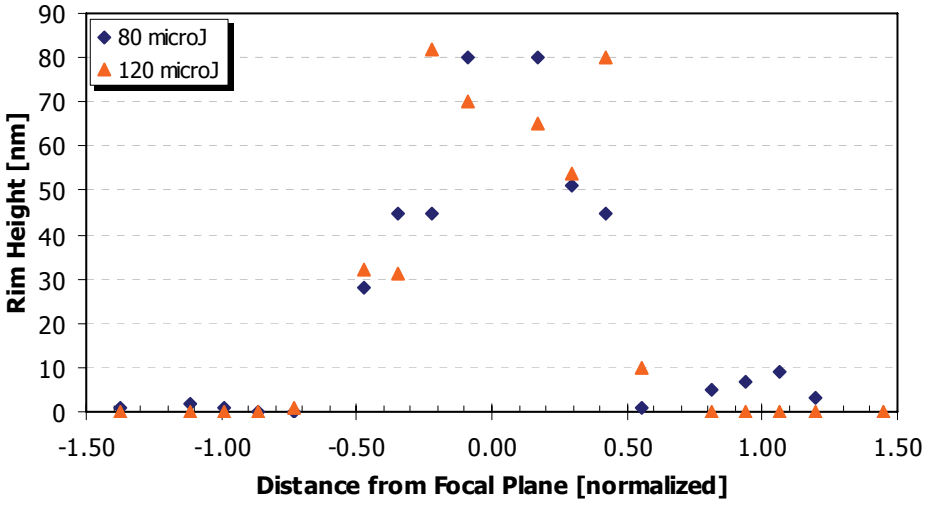

Figure 3-14: Variation in rim heights as the glass sample moves closer to the focal plane. The x-axis is normalized by the Rayleigh range. Typically, rims are found to be the highest at the focal plane, z=0. There is an unavoidable large scatter in the data (approx. 20-30 nm), because of non-uniform thickness of the rim surrounding the crater.

This trend cannot be easily modeled using a simple equation, since the rim formation is a result of complex physical phenomena. However it is plainly visible from the experimental data that the rim heights are the highest when the sample surface is at the focal plane, and then the rim heights keep reducing as the sample moves either towards or away from the focusing lens. Since the fluence is highest at the focal plane, accordingly, the ablation depth is the largest and the crater size is

the smallest here. The melt zone is therefore larger in this case. It has to spread around a smaller crater perimeter in a relatively short period of time, leading to a higher rim.

In this particular case, the rims vary between 80 nm to rimless craters. The fluctuation is of the order of about 30 nm.

Rim heights below 20 nm in my experiments are considered to be almost rimless. The rim heights are quite scattered because sometimes it is difficult to clearly differentiate between the rim and the splash due to the scattered debris. The main issue of concern in this thesis is the rim around the crater formed due to resolidification of the molten layer. Logically, this rim seems to be the main culprit behind the lack of smoothness in multishot ablation channels. The debris created during the ablation process gets loosely stuck to the glass surface and can be easily gotten rid of by etching with mild NaOH for a few minutes.

To better understand the trend, we normalize the rim height by the crater depth for each crater. The variation in the normalized rim height as the lens moves closer to the target surface is shown in Figure 3-15 below:

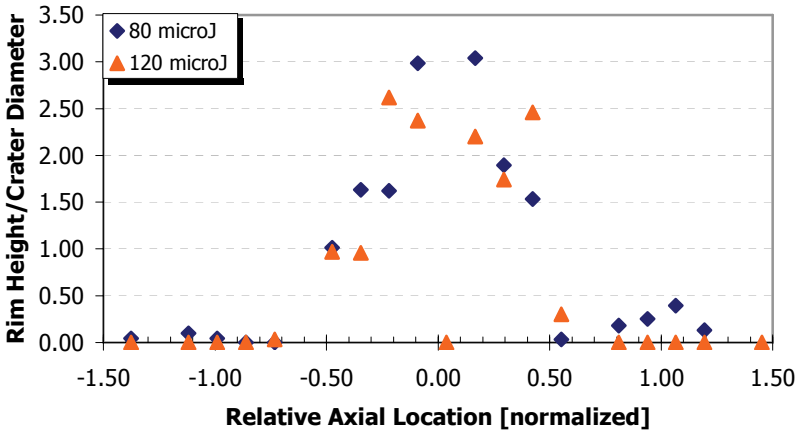

Figure 3-15: Variation in the rim height to crater depth ratio with the distance of the sample surface from the focal plane. The ratio is highest at the focal plane, and decreases as the sample moves away from the focal plane in either direction.

As in case of Figure 3-10, the rim height/crater depth is the highest at the focal plane and then it decreases as the sample moves away from the focal plane in either direction.

Similar ablation experiments with single laser pulses are performed on borosilicate glass, using plano-convex lenses of different focal lengths (f = 50 mm, 100 mm, 250 mm) (and hence different Numerical Apertures), with different pulse energies and at varying distances from the focal plane. The incoming beam diameter is the same as that from the amplifier exit. All these different experimental settings serve to change the crater morphology (diameter, depth, rim height) by changing the fluence and focusing conditions.

The data so obtained is compiled into separate graphs and is available in the Appendix C. The trends seen with all the different focusing lenses are similar to the ones discussed above for f = 100 mm. A summary of all the compiled data is given in Figure 3-16. This helps to give an idea of the orders of magnitude involved.

NA	**f [mm]**	**w_1 [μm] (max^m)**	**h [nm] (max^m)**	**b [nm] (max^m)**	**b/h (max^m)**
0.08	50	24	700	180	0.45
0.04	100	33	400	80	0.22
0.02	250	100	450	20	0.15

Figure 3-16: Summary of measured crater dimensions for different experimental set-ups. The highest values have been listed in this table to give an estimate of the orders of magnitude involved.

NOTE: *NA* = Numerical Aperture, f = focal length, w_1 = focused beam spot size, h = crater depth, b = rim height, b/h = rim height/crater depth ratio.

3.5.4 Error Analysis

The crater width is measured using images from the optical microscope and from the AFM scans. The accuracy of the readings is ± 0.2 μm. The limitation in the measurement is because of the spread out crater rims which make it difficult to pinpoint the exact edge of some of the single-shot ablation craters. The relative error is therefore typically of the order of ± 1%.

Typical error bars for measurement of crater depth are shown in Figure 3-17. The average accuracy for the depth measurement is about 20 nm. The uneven bottoms and the presence of some debris in some craters results in this fluctuation in measurement. The relative error therefore varies from about 4 to 8% for different crater depths.

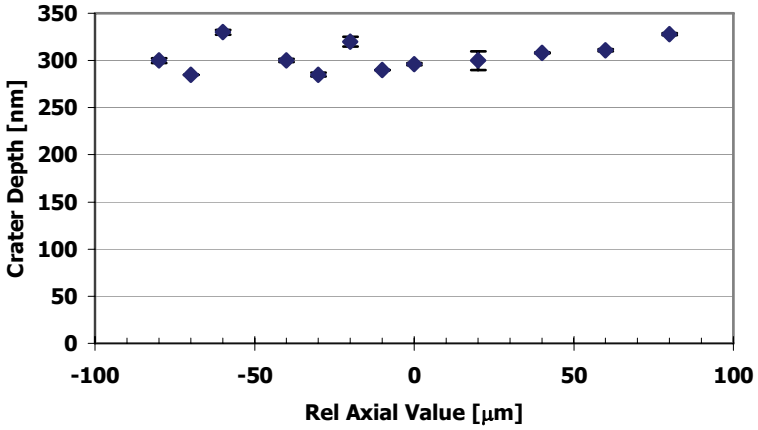

Figure 3-17: Typical error bars for crater depth measurement as the lens moves closer to the glass sample. In this case, the focal length is 50 mm, pulse energy is 8 μJ, beam spot size is approximately 6.2 μm.

Figure 3-18 shows typical error bars in the measurement of rim heights of single shot craters. The fluctuation is about ± 20 nm. However this value changes a lot depending on the experimental conditions, and varies between 10 nm to 60 nm. The presence of debris, and the non-uniformity of the rims leads to this high error. For a typical 10 to 100 nm rim height, this implies a relative error ranging from 20 to 200%. In most cases, the measurements and analysis are done based on a physical understanding of the process. Data points with very high relative error have not been used for the overall analysis.

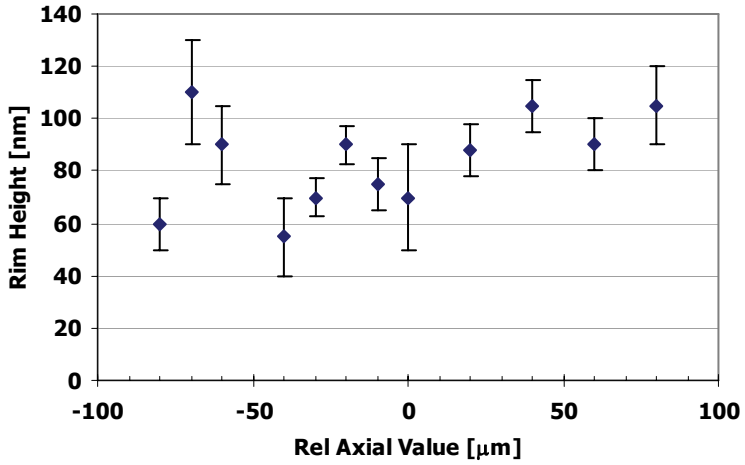

Figure 3-18: Typical error bars for crater rim height measurement as the lens moves closer to the glass sample. In this case, the focal length is 50 mm, pulse energy is 8 μJ, beam spot size is approximately 6.2 μm.

The error measurements for the crater depth and rim height shown in the plots above are mathematically combined to find the error for the rim height/crater depth ratio, and some typical data is plotted in Figure 3-19. We see a very high fluctuation in the data. Only data-points with errors that can be physically justified have been used for the overall analysis.

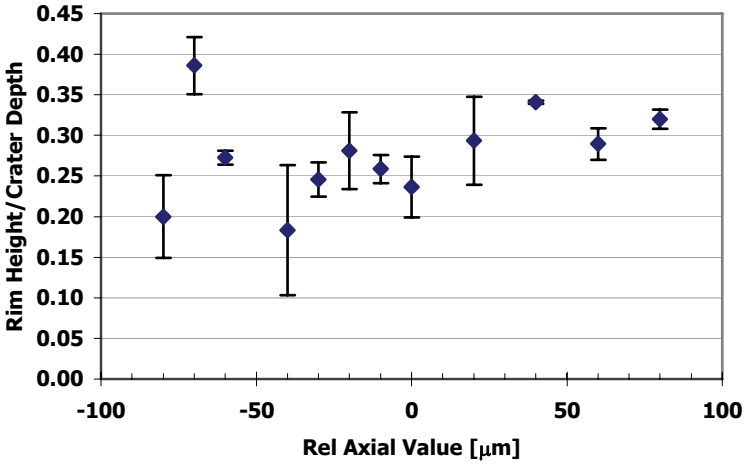

Figure 3-19: Typical error bars for rim height/crater depth ratio as the lens moves closer to the glass sample. In this case, the focal length is 50 mm, pulse energy is 8 μJ, beam spot size is approximately 6.2 μm.

3.6 Overall Conclusions from the Entire Dataset

As per the discussion about the crater rims in section 1.2.3.1, we expect to see a relationship between the rim height and the crater width and depth. Accordingly, we plot the variation in the rim height with the crater diameter and with crater depth in Figure 3-20 and Figure 3-21 below. This dataset includes data for different ways of changing the crater dimensions including

- different pulse energies
- different beam spot sizes using different focusing conditions, and
- different beam spot sizes using different distances from the focal plane

There is no clear trend of how the rim height changes with the crater diameter and depth.

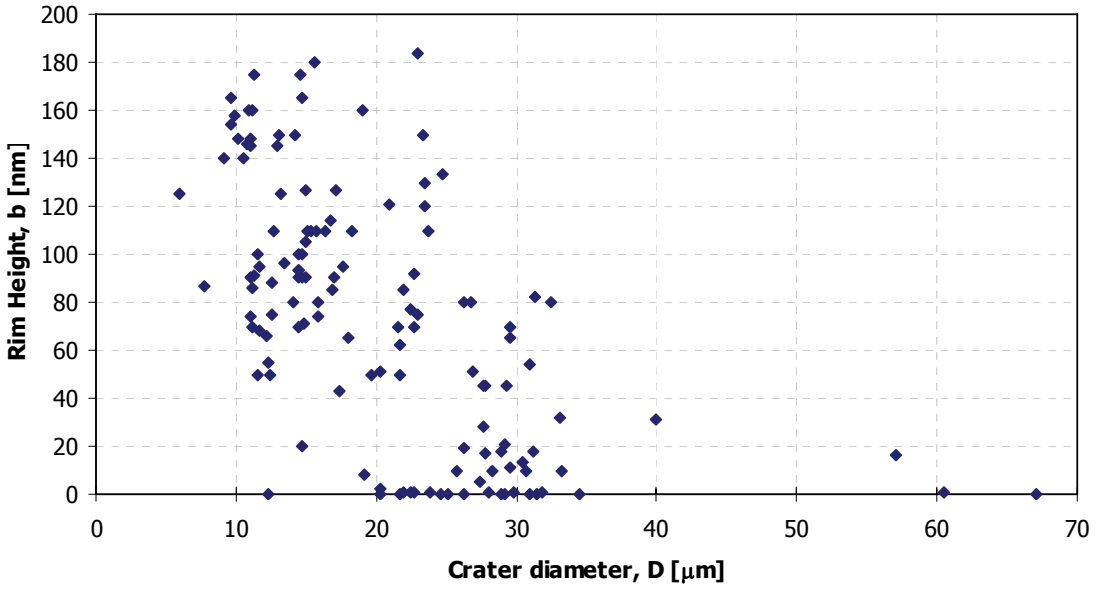

Figure 3-20: Rim Height versus Crater Diameter. No particular trend seen. Data includes different focusing lenses, different pulse energies and different locations of the glass sample from the focal plane of the focusing lens.

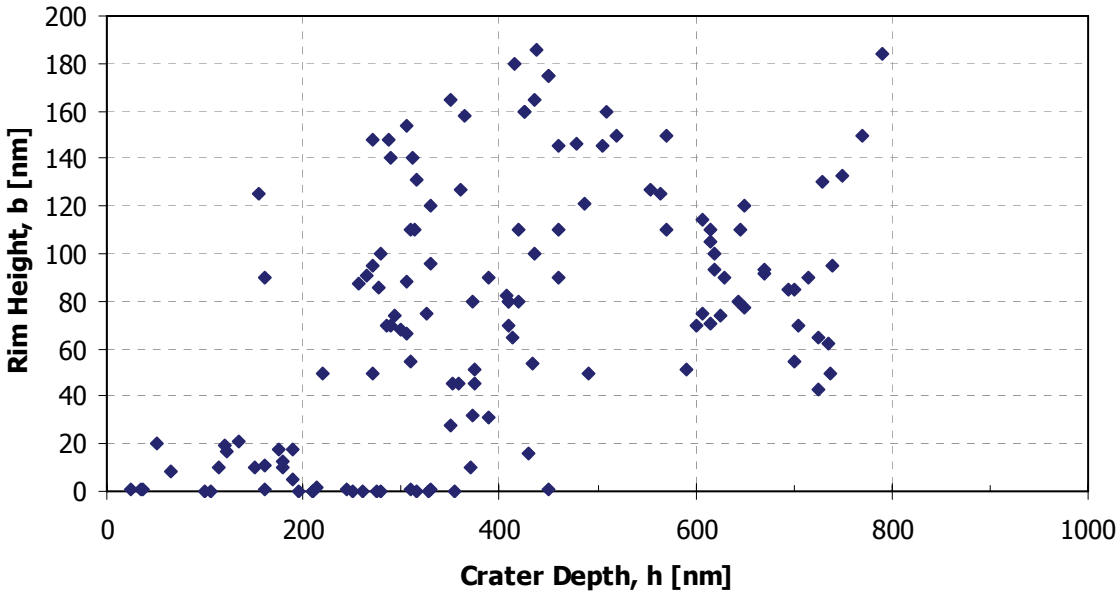

Figure 3-21: Rim Height versus Crater Depth. No particular trend seen. Data includes different focusing lenses, different pulse energies and different locations of the glass sample from the focal plane of the focusing lens.

Next, for each crater, the ratio of the rim height to crater depth is plotted against the crater depth (Figure 3-22). A distinct inverse relationship is seen between the three parameters. The plot shows that the crater width, depth and rim height are interconnected.

A detailed comparison between Figure 3-22 and Figure 3-23 shows that the possible relationship between b/h and D is:

$$b/h \propto 1/D^2$$

or

Rim height/Crater Depth (b/h) is inversely proportional to the square of Crater Width (D^2)

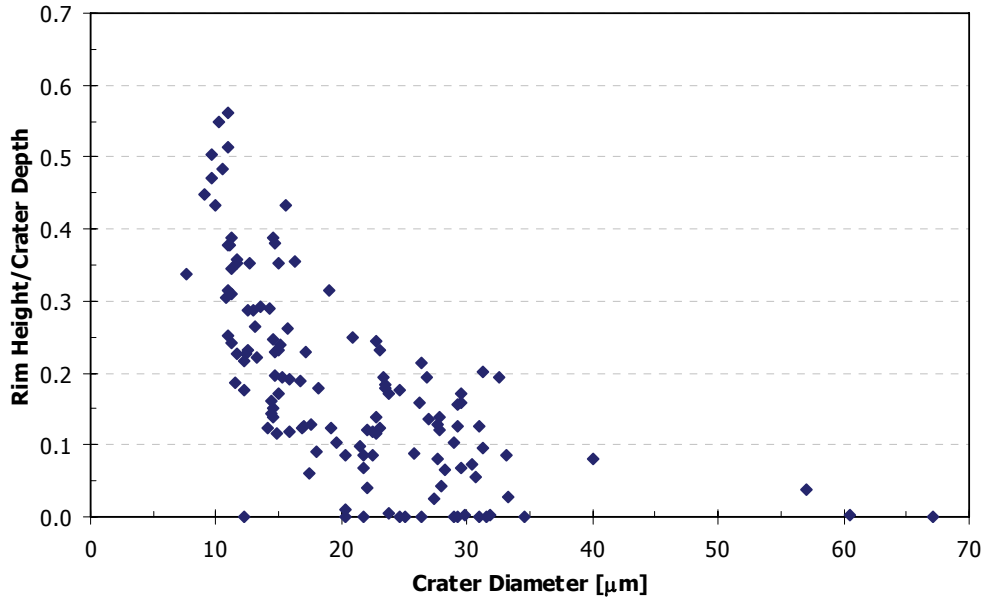

Figure 3-22: Rim Height/Crater Depth versus Crater Diameter. Data includes different focusing lenses, different pulse energies and different locations of the glass sample from the focal plane of the focusing lens. An inverse relationship is seen.

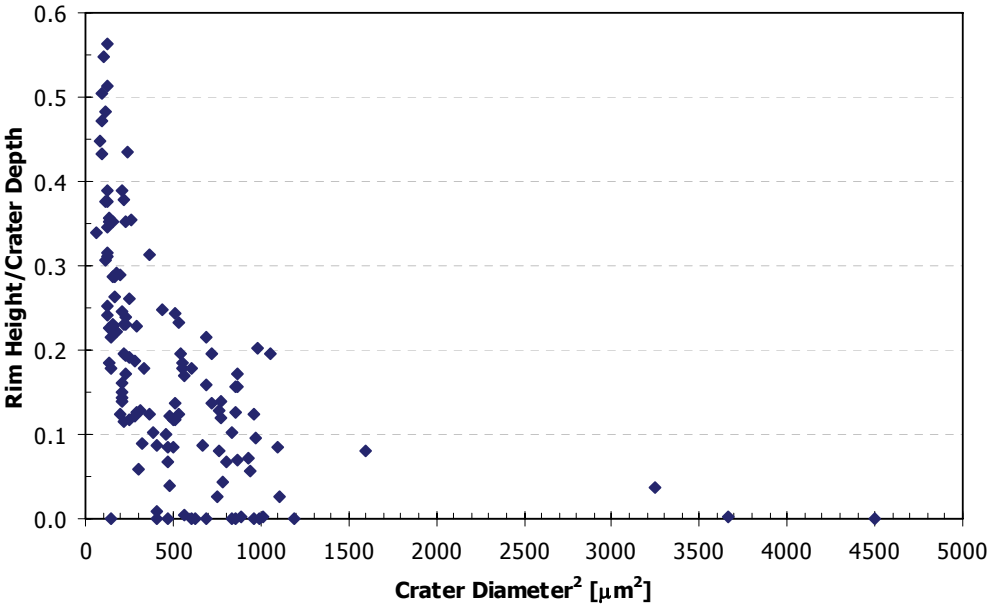

Figure 3-23: Rim height/crater depth versus (crater diameter)^2. Data includes different focusing lenses, different pulse energies and different locations of the glass sample from the focal plane of the focusing lens. An inverse '1/x' relationship is seen.

4 Ablation with Top-Hat Beam Profile

Surface ablation of borosilicate glass is carried out using high energy single femtosecond pulses, which have been reshaped by truncating the incoming Gaussian beam with a circular aperture. The results are compared with the results from the previous chapter (ablation with the Gaussian beam profile), in order to understand the effect of reshaping the beam into a top-hat spatial profile. Explanation has been offered for the observations, though it needs to be validated using appropriate modeling.

4.1 Experimental Setup & Procedure

The experimental set-up is the same as in Figure 3-1 except that a circular aperture is placed in the front focal plane of the lens, (ie. a distance f before the lens). Both the aperture and the lens are on a translation stage arranged to move in the axial direction in small increments. The borosilicate glass sample is fixed on an x-y-translation stage and is positioned normal to the direction of the incident laser beam. The schematic is shown in

Figure 4-1.

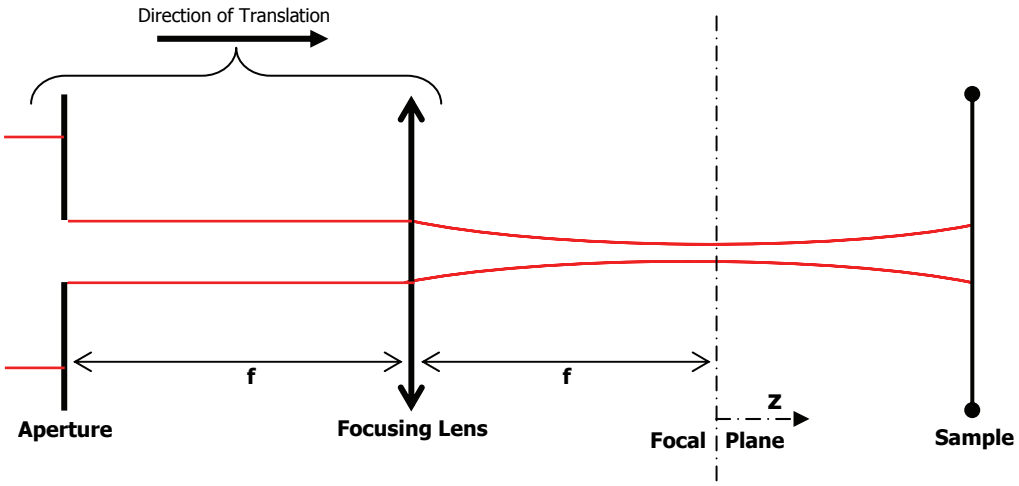

Figure 4-1: Schematic of Experimental Setup. The circular aperture is placed in the front focal plane of the achromatic focusing lens. The aperture and lens are fixed on the same translation stage and move towards the glass sample surface in controlled increments.

The experiment is set up in such a way that we should get an Airy disk at the focal plane, which has characteristics of the far-field regime. As we move outside the Rayleigh range of the focused beam spot in either direction, the beam profile should become a mixture of an Airy disk and a top-hat (see section 2.2.2). In the near-field region, the profile should look more like a top-hat (Figure 2-6). This set-up can be modeled based on Fresnel diffraction in the near-field region and Fraunhoffer diffraction in the far-field (at the focal plane).

This has been verified by mapping the spatial intensity profile of the beam using a beam profiler, as can be seen in Figure 2-7. Note that since a hard edge aperture is used to truncate the beam, this leads to diffraction fringes in the beam profile that can be clearly seen in the images.

Single shot ablation experiments are carried out with different laser pulse energies ranging between approximately 5 μJ to 500 μJ, and with two different *NA* lenses. Also, the variation in crater morphology is studied while moving the target away from the focal plane of the lens.

An achromatic doublet is used as the focusing lens in this set of experiments in order to ensure that all the wavelengths get focused at the same axial distance from the lens. This is necessary in order to achieve the best possible top-hat beam profile.

Keeping the laser energy fixed, the aperture and focusing lens are translated towards the sample surface in controlled small step sizes (Figure 4-1), and five single shot ablation craters are made on the sample surface per axial position, to ensure statistical consistency. The single shot craters are at least 200 microns apart from each other, to make sure there are no diffraction effects because of the craters being too close [15].

All experiments are performed in air at atmospheric pressure.

4.1.1 Data Available

Single shot ablation craters were made on the surface of borosilicate glass with the following experimental parameters:

f = 20 mm, *NA* = 0.28, *E* = 7.7, 12.5, 15.2, 20.5, 24 μJ
f = 50 mm, *NA* = 0.035, *E* = 50, 80, 296, 409 μJ

where *f* = focal length; *NA* = Numerical Aperture; *E* = pulse energy

4.2 Discussion about the observed trends

Trying to simulate the behavior of the beam profile at and around the focal plane is a very involved process, since we expect to see an Airy disk at the focal plane, but a combination of a top-hat and an Airy disk beyond the Rayleigh range of the focused beam spot. The area of interest is this combination of the two different intensity distribution profiles.

4.2.1 Crater Width

At the focal plane, the beam profile is an Airy disk, rather than a Gaussian distribution. For an aperture diameter $2w_0$ = 3.5 mm and a focusing lens with focal length *f* = 20 mm (*NA* = 0.28),

Radius of Airy disk = $w_1 = 1.22\ \lambda f/2w_0$ = 5.4 μm.

Yura et al [40] show that for the same aperture to beam diameter truncation ratio, the radius of the beam spot size at the focal plane is

$w_1 = 1.28 f\lambda/D$

= 1.28 * 20 * 0.780 / 3.5 = 5.7 μm

This spot size calculated this way is about 5% larger than that calculated using the Airy Disk assumption and thus the two theories corroborate.

On the other hand, beam waist expected for a Gaussian profile is
$w_1 = f\lambda/\pi w_0 = 2.8$ μm

By measuring crater sizes created by multiple pulse energy settings, and using the method used in section 3.5.1 for estimating the beam spot size, we find that the profile at the focal plane is indeed an Airy disk.

Sample data for variation of crater diameter with axial displacement is shown in Figure 4-2 below. As the focal plane moves inside the sample, the beam profile starts approaching a top-hat. For an incident laser beam with a fixed given pulse energy, the radius of a top-hat is $1/\sqrt{2}$ times the radius of a Gaussian. Accordingly, away from the focal plane, the beam spot size and hence the crater size will be much smaller than that predicted for a usual Gaussian beam, leading to a smaller crater size. This is exactly what we see in the experiment.

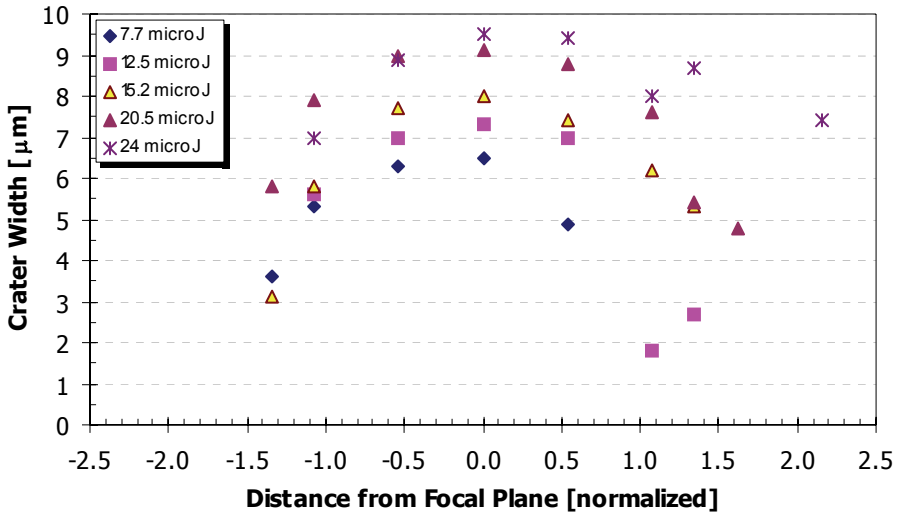

Figure 4-2: Variation in the single shot ablation crater width as the lens moves towards the glass surface. The x-axis is normalized by the Rayleigh range. The craters are widest at the focal plane, 'z=0'. Beam profile = 'top-hat', *NA* = 0.28, aperture diameter = 3 mm, beam spot size ≈ 5 μm. This trend is different from that seen for ablation with a Gaussian beam profile.

Note that we do not need to account for the M^2 propagation factor while working with this set-up, since the aperture acts like a spatial filter and cleans out

the beam to a certain extent, thus reducing the M^2 factor and hence reducing the divergence from a perfect Gaussian TEM_{00} beam.

All craters are very circular when the truncated beam is used for ablation. In the case of the Gaussian beam, the ellipticity of the craters was used to estimate the focal plane. This can not be done when the aperture is in place, and the focal plane needs to be estimated by looking for other symmetry in the measurements. In Figure 4-2, the focal plane seems to lie where the craters become the widest.

4.2.2 Crater Depth

The crater depth is seen to be the highest at the focal plane and the craters become shallower as the target moves away from the focal plane (Figure 4-3).

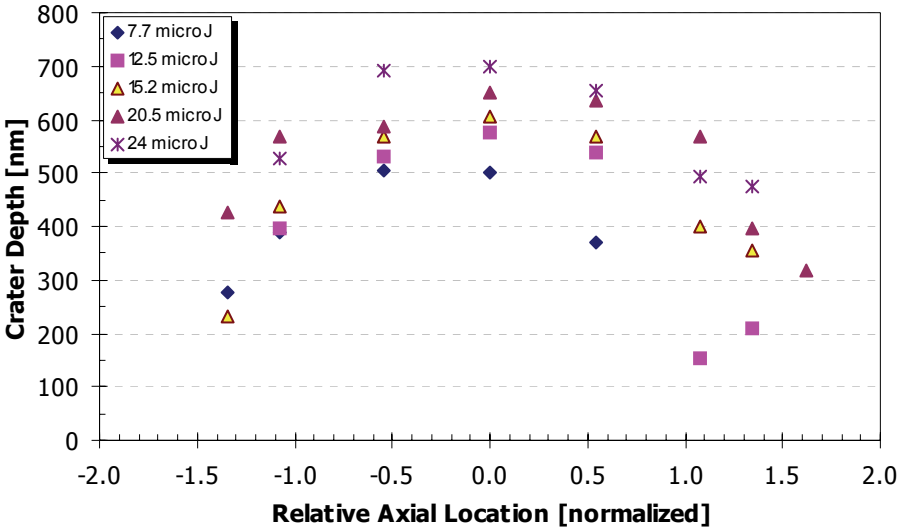

Figure 4-3: Variation in the single shot ablation crater depth as the lens moves towards the glass surface. The x-axis is normalized by the Rayleigh range. The craters are deepest at the focal plane, 'z=0'. Beam profile = 'top-hat', *NA* = 0.28, aperture diameter = 3 mm, beam spot size ≈ 5 μm. The trend is the same as that for ablation with a Gaussian beam profile, although the reasoning is more involved.

The trends for the crater width and depth can be understood correctly only if the change in fluence and the beam spot size can be mapped as the distance

between the lens and the sample surface decreases. This can be done by employing the now-familiar equations:

$$D^2 = 2w_0^2 \ln\left(\frac{F_o^{avg}}{F_{th}^{N=1}}\right) = 2w_0^2 \ln\left(\frac{E}{E_{th}}\right) \quad \textbf{...(4.1)}$$

$$h_a = \alpha_{eff}^{-1} \ln\left(\frac{F_0^{avg}}{F_{th}^{N>1}}\right) \quad \textbf{...(4.2)}$$

where h_a is the ablation depth, α_{eff}^{-1} is the effective optical penetration depth, and equals 240 nm when ablating in air [15]. F_0 denotes average fluence; $F_{th}^{N>1}$ is the multishot threshold fluence for borosilicate glass calculated to be equal to 1.7 J/cm^2 (independent of atmospheric conditions). D is the crater width and w_0 is the beam spot size (radius) at that axial location. $F_{th}^{N=1}$ is the single-shot threshold fluence for the substrate calculated to be equal to 2 J/cm^2.

Variation in average fluence as a function of the distance of the lens from the target can be estimated by using equation 4.2 with the measured values of h_a as a function of 'z'. Figure 4-4 below shows that the fluence is highest at the focal plane and decreases as the lens moves further from or closer to the sample.

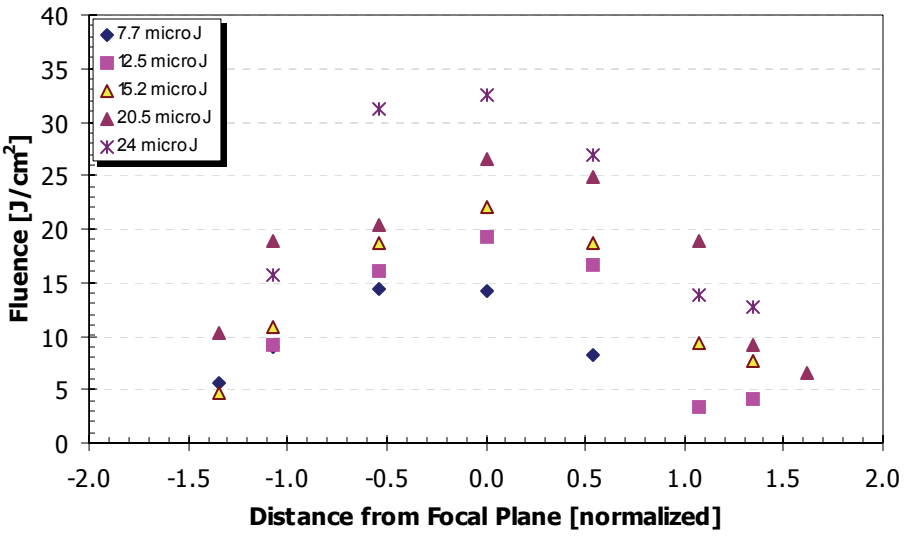

Figure 4-4: Variation in fluence as the lens moves towards the glass sample. The x-axis is normalized by the Rayleigh range. The fluence is the maximum at the focal plane, as expected. Beam profile = 'top-hat', *NA* = 0.28, aperture diameter = 3 mm, beam spot size ≈ 5 μm.

Similarly, equation 4.1 can be used with the measured values of crater diameter D and the above-calculated values of fluence F_0^{avg} to model how the beam spot size w_0 changes as the distance between the lens and the sample changes. Although the equation is originally derived for the case of ablation by a Gaussian beam, it is safe to assume that the trend of the variation in diameter for craters made by a top-hat beam would be similar. We find that the spot size stays almost constant till the Rayleigh range (Figure 4-5). With higher energies and thus more data points, the beam spot size is seen to increase beyond the Rayleigh range, because of beam diffraction.

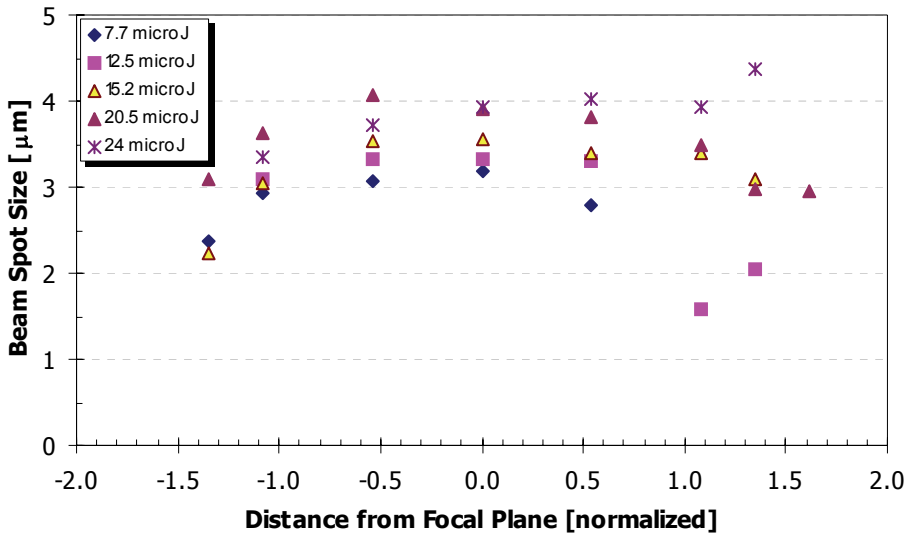

Figure 4-5: Variation in beam spot size as the focusing lens moves closer to the glass surface. The x-axis is normalized by the Rayleigh range. The spot size is the maximum at the focal plane and decreases as the sample moves away from the focal plane in either direction. At a relatively large distance from the focal plane, the spot size starts increasing again. Beam profile = 'top-hat', *NA* = 0.28, aperture diameter = 3 mm, beam spot size ≈ 5 μm.

Unlike the Gaussian beam profile, the spot size does not increase monotonically as we move away from the focal plane, because the increase in spot size because of diffraction is compensated by the decrease due to the transition of the beam profile from an Airy disk into a top-hat.

Theoretical modeling of fluence distribution is more involved and we depend on the estimated trend for the fluence for varying axial location of the sample as done in Figure 4-4. The peak fluence at the focal plane causes the crater width and depth to be the highest at the focal plane. The decreasing fluence as the focal plane moves farther from the glass surface justifies the monotonically decreasing crater dimensions away from the focal plane.

4.2.3 Crater Rim Height

The trend in rim heights measured for the case of single shot ablation craters made with a top-hat beam of beam spot size radius 5 μm is shown in Figure 4-6.

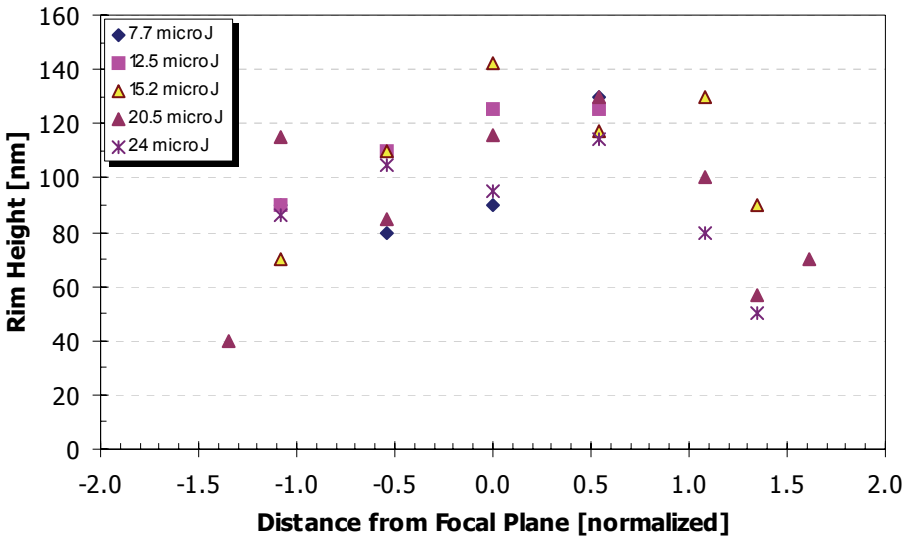

Figure 4-6: Variation in crater rim height as the focusing lens moves closer to the glass surface. The x-axis is normalized by the Rayleigh range. The rim height is maximum at the focal plane (Airy disk pattern) and decreases as the sample moves away from the focal plane in either direction (top-hat pattern). Beam profile = 'top-hat', *NA* = 0.28, aperture diameter = 3 mm, beam spot size ≈ 5 μm.

The rim heights are typically the highest when the focal plane is at the glass surface. This is similar to what was observed in case of the Gaussian craters (Figure 3-14).

In Figure 4-7, we plot the ratio of the rim height to the crater depth against the axial displacement for each crater, to check for any significant trends. It seems to be steady within the Rayleigh range and decreases beyond it indicating that the rim height and crater depth decrease at the same rate initially and then the rim height starts decreasing more sharply.

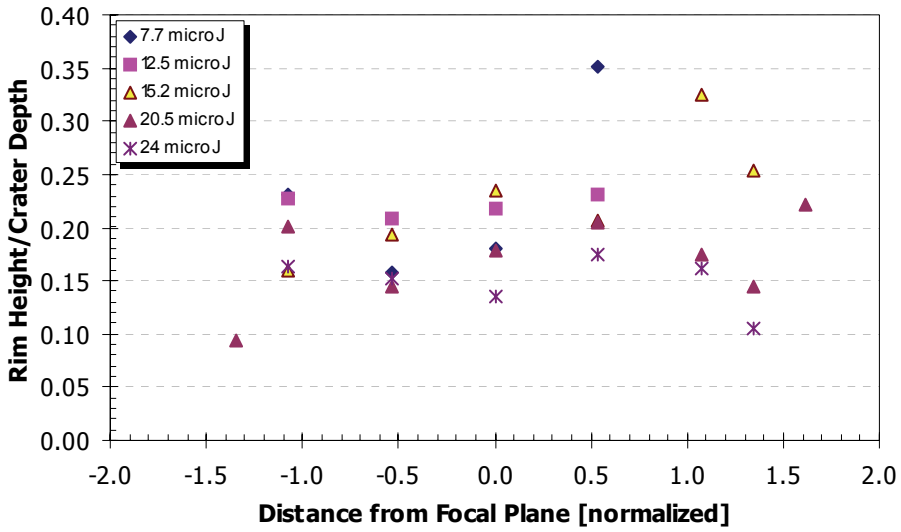

Figure 4-7: Variation in rim height/crater depth ratio as the focusing lens moves closer to the glass surface. The x-axis is normalized by the Rayleigh range. The ratio seems to be steady till the Rayleigh range and then seems to decrease. This is in contrast to the trend seen with the Gaussian beam profile which is lowest at the focal plane (Figure 3-15). beam profile = 'top-hat', *NA* = 0.28, aperture diameter = 3 mm, beam spot size ≈ 5 μm.

Graphical trends for more data points are shown in the Appendix E. The trends for the rim height seem to be mostly consistent from experiment to experiment although a large scatter is seen the data. This is because of the difficulty of delineating the cause of the rim (melt or debris), especially in case of wider craters.

NA	**f [mm]**	**w_1 [μm] (max^m)**	**D [μm] (max^m)**	**h [nm] (max^m)**	**b [nm] (max^m)**	**b/h (max^m)**
0.035	50	18	37	500	40	0.13
0.035	50	18	27	300	40	0.15
0.28	20	5	9	700	130	0.23

Figure 4-8: Summary of experimental data for 'top-hat' Single Shot Ablation Craters

NOTE: *NA* = Numerical Aperture, *f* = focal length, w_1 = focused beam spot size, *D* = crater diameter, *h* = crater depth, *b* = rim height.

4.3 Comparison between 'Gaussian' and 'Top-Hat' Craters

As shown in section 3.5.4, the rim height is a function of the crater width and crater depth. Figure 4-9 below plots the variation in rim height/crater depth with the crater diameter. The crater diameter is changed in the dataset by the following methods:

- different pulse energies
- different distances from the focal plane, and
- different beam spot sizes using different focusing conditions.

The diamonds in the graph represent the craters ablated with the Gaussian beam profile, as also shown in Figure 4-9. The triangles represent all the craters ablated with the sharply truncated Gaussian beam. Among these data points, those which are beyond the Rayleigh range (where the beam profile resembles a top-hat) are represented with the crosses.

As a trend, the rim height/crater depth ratio for the top-hat craters is lower than that for the Gaussian craters. Among the top-hat craters themselves, the ratio seems to decrease with increasing crater width, as is the case for the Gaussian craters.

It is easy to see that the rim height/crater depth ratio for single shot ablation craters is more a function of the crater width than of the beam profile.

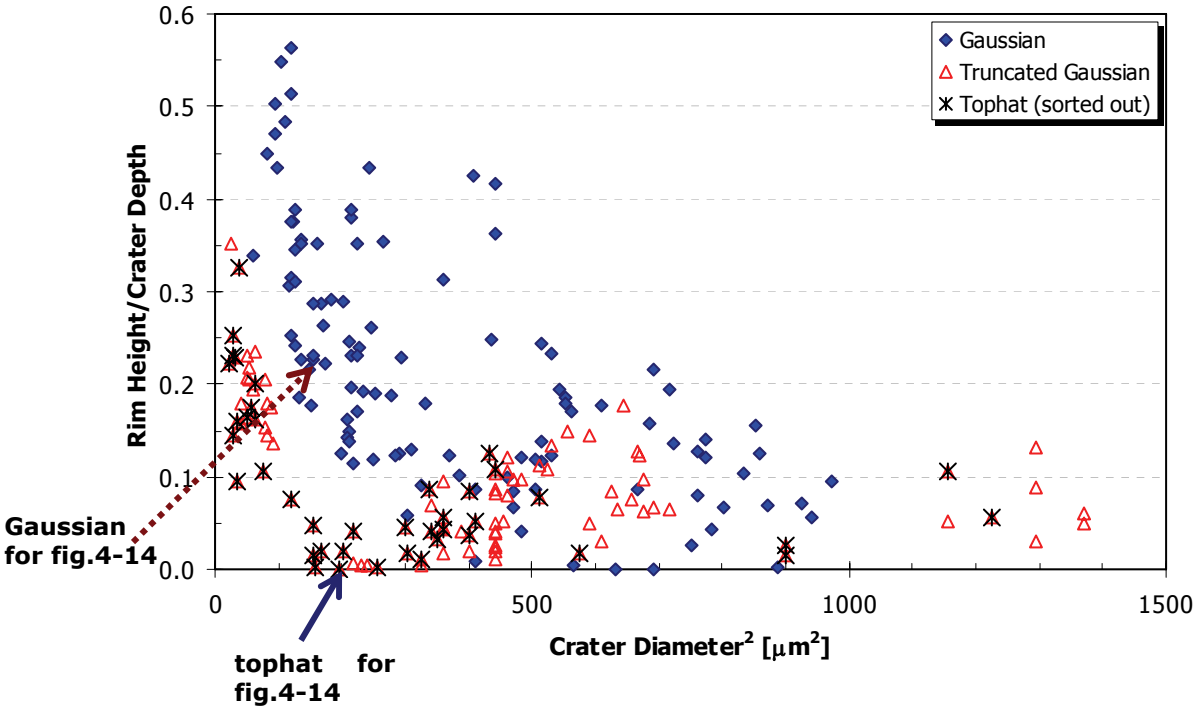

Figure 4-9: Variation in ratio of rim height by crater depth (b/h) with the square of crater diameter (D^2). Diamonds indicate craters ablated with Gaussian beam profile, triangles indicate craters ablated with a largely truncated Gaussian beam, and the crosses are the craters with the glass surface some distance away from the focal plane, where the beam profile almost resembles a top-hat profile. The arrows indicate the datapoints which have been shown in Figure 4-10.

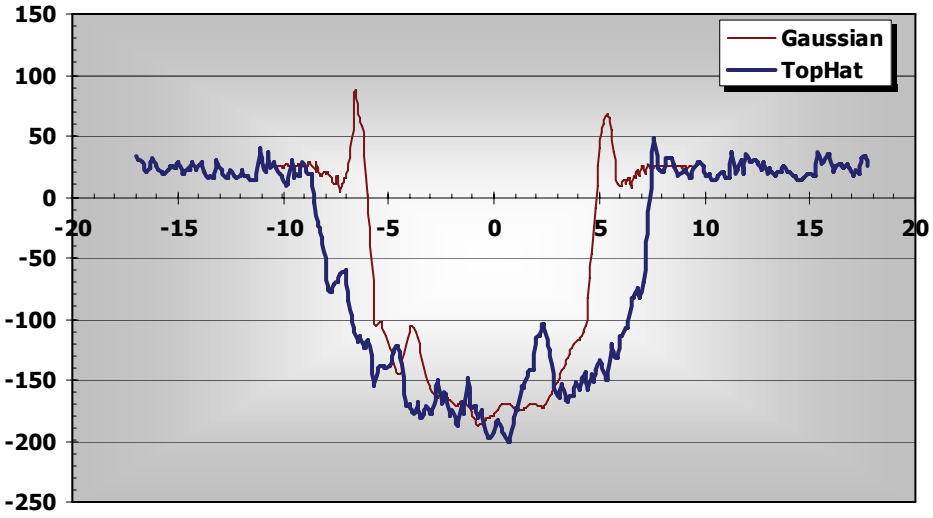

Figure 4-10: For craters with same depth = 220 nm and near threshold fluence, rim height is lower for top-hat crater than for the Gaussian crater. top-hat crater: f = 50 mm, E = 50 μJ, depth = 220 nm, width = 16 μm. Gaussian crater: f= 50 mm, E = 20 μJ, depth = 220 nm, width = 12.4 μm. The x-axis is in μm, y-axis is in nm. The data-points are indicated by arrows in Figure 4-9.

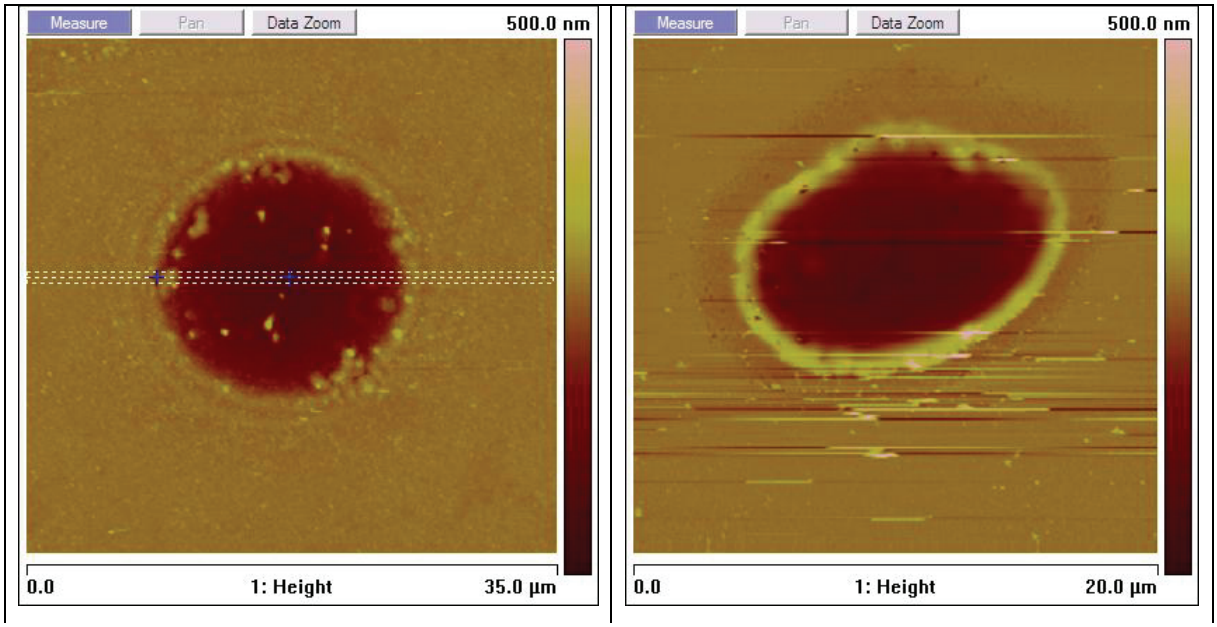

Figure 4-11: AFM images of the top-hat and Gaussian craters compared in Figure 4-10. The top-hat craters are always circular and have a uniform rim as compared to the Gaussian craters

Figure 4-10 compares the AFM cross-sections of a typical case of a top-hat and a Gaussian crater with similar crater depths, implying similar laser fluences. The rim height is seen to be lower for the top-hat crater. The AFM images of the two craters are again shown in Figure 4-11.

In this project, a tight circular aperture is used to truncating the Gaussian beam to create the top-hat beam profile. Figures 16 till 19 below give a comparison between typical trends for craters ablated by the truncated and untruncated Gaussian beam. The difference in trends for the crater width and for the rim height/crater depth variation as a function of the axial displacement proves that reshaping the spatial beam profile does affect the crater morphology. This is also validated by the crater width calculations for the truncated Gaussian beam, which shows that the crater width at the focal plane corresponds to that for an Airy disk beam profile.

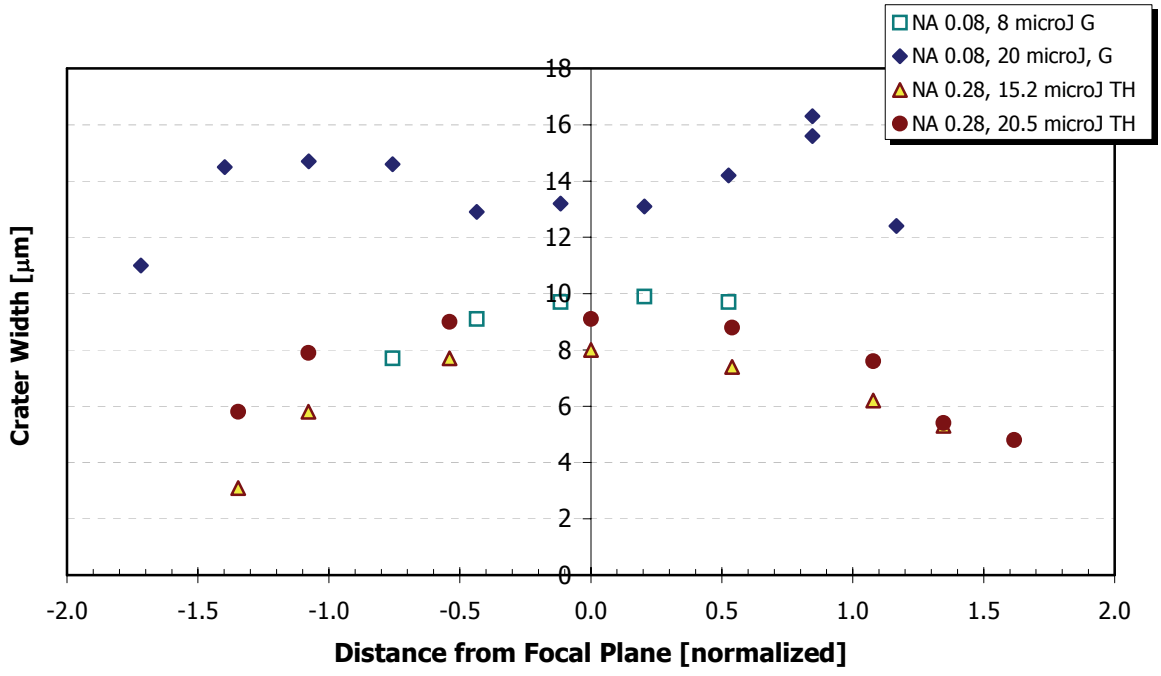

Figure 4-6: Variation in crater width with distance from focal plane. The x-axis is normalized by the Rayleigh range. The trend is different for the Gaussian and top-hat craters.

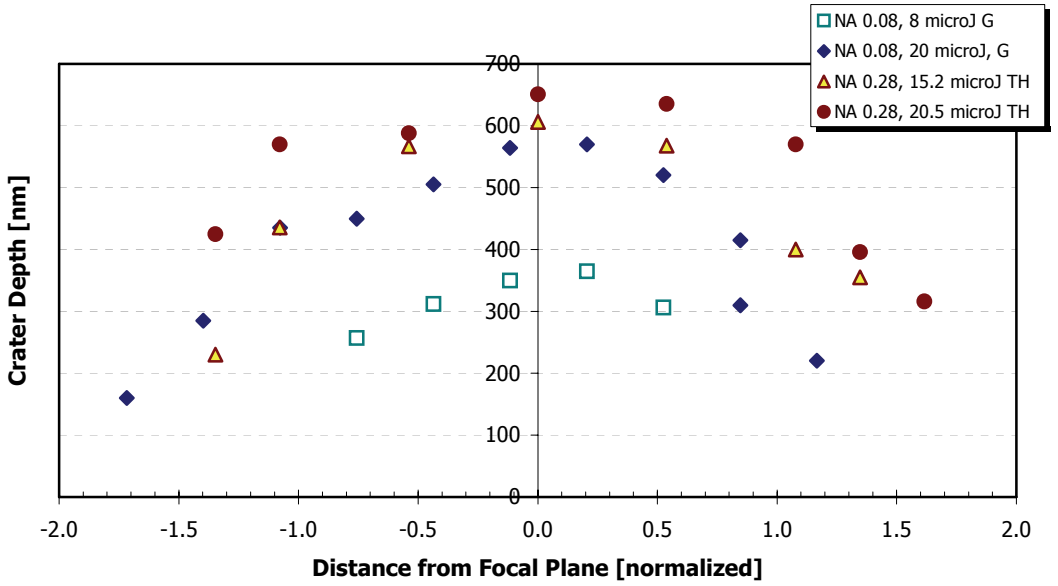

Figure 4-12: Variation in crater depth with distance from focal plane. The x-axis is normalized by the Rayleigh range. In case of both the Gaussian and the top-hat beam profiles, the crater depth decreases with increasing distance from the focal plane. In all cases shown, beam spot size ~ 6 micron.

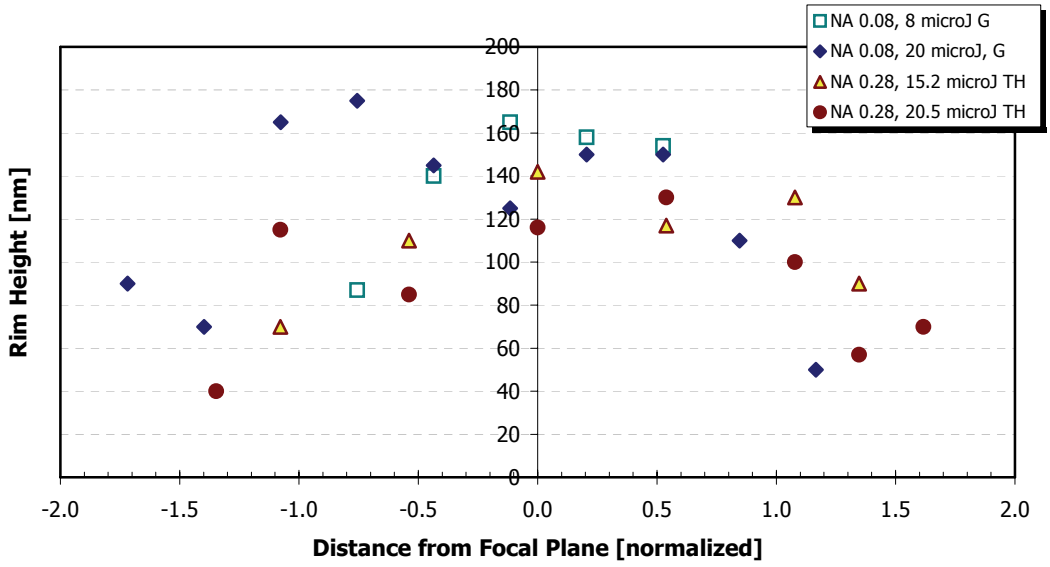

Figure 4-13: Rim height decreases for both Gaussian and top-hat beam profiles as we move away from the focal plane. The x-axis is normalized by the Rayleigh range. In all cases shown, beam spot size ~ 6 micron.

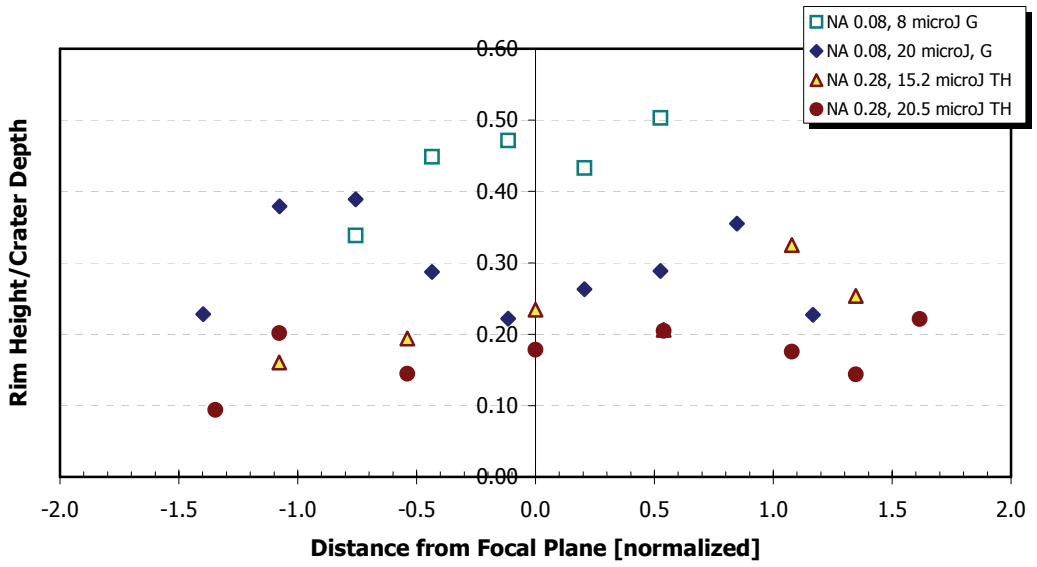

Figure 4-14: rim height/crater depth Ratio decreases as the beam profile changes from airy disk to top-hat. The x-axis is normalized by the Rayleigh range. It behaves in the inverse fashion when the beam profile stays Gaussian all through. This shows that beam shaping is an effective method for controlling the crater rim height development. In all cases, spot size ~ 6 μm, depth ~ 700 μm

Hence Figure 4-9 and Figure 4-14 show that truncating the Gaussian beam with a sharp aperture to create a top-hat does affect the crater morphology, and the rim height/crater depth for the top-hat profile is lower than for the Gaussian profile, as originally expected. As a conclusion, the beam shaping does indeed affect the rim formation process during ablation with femtosecond laser pulses.

5 Concluding Remarks

5.1 Summary of Major Results and Conclusions

5.1.1 Experimental Procedure

- **Spatial Reshaping of Laser Beam from Gaussian into Top-Hat:** By truncating the incoming femtosecond beam with a very small circular aperture, we show that we can successfully reshape the Gaussian laser beam into a top-hat spatial profile. In our case, we use a 3.5 mm diameter aperture for a 22 mm diameter Gaussian beam. This method is inexpensive and easy to implement, but is not efficient in terms of energy. Hence this technique serves as a good method for showing our proof of concept, but is not good to be used on a commercial scale.

- **Improving Laser Beam Shape by Slight Truncation:** The laser beam transverse cross-section and the resulting ablation craters can be made circular by placing a low truncation ratio circular aperture before the focusing lens in the beam path. It acts like a crude spatial filter and removes the higher order Fourier transform components from the beam to a certain extent. These craters have a homogenously distributed rim, as compared to the uneven rims of the elliptical craters made by ablation with an untruncated Gaussian laser pulse. The calculated energy density in the side-lobes of the Airy disk pattern is expected to be less than 1% of the maximum energy and thus does not affect the ablation results.

- **Effect of Focal Plane Location:** We have experimentally validated the fact that the crater morphology (crater width, depth and rim height) changes depending on the position of the sample surface relative to the focal plane of the focusing lens. It is worth noting that the crater rim height, in general, decreases as the focal plane of the focusing lens moves inside the sample surface (trend shown in Table 1). This happens probably because the high fluence in the bulk of the substrate causes breaking of bonds inside, thus

compressing the material. This, in turn, causes the crater to sink below the surface level, without forming a well-defined rim. Hence, for a given experimental setup, the sample surface can be positioned such that it can take advantage of this physical phenomenon, thus resulting in reduced crater rim heights. Also, machining should be avoided with the sample surface beyond the focal plane, to avoid any beam distortion effects by the dissociation of air at the focal point.

5.1.2 Experimental analysis

- **Rim Height Relation With Crater Size: $b/h \propto 1/D^2$**: The crater rim height is shown to be a function of the crater width and depth. It is known that the crater depth is solely dependent on the fluence, while the crater width is a function of both the fluence and the beam spot size. We measure the dimensions of the crater and the rim for different combinations of fluence and spot size. ***Our experiments indicate that the ratio of the rim height to the crater depth is inversely proportional to the crater width.***

- **Affect of the Top-Hat Beam Shape:** Comparison of trends between the craters ablated by the untruncated (Gaussian) and the truncated (top-hat) beam profiles shows that beam shaping influences the crater morphology [Table 1].

  In case of ablation with the Gaussian pulse profile, the spatial beam profile remains Gaussian as the sample surface moves away from the focal plane (in either direction). Although the absolute rim height becomes smaller, the rim height to crater depth ratio increases, implying that the rim height decreases more slowly as compared to the decrease in the crater depth.

  On the other hand, when working with the truncated laser beam, the pulse profile transitions from an Airy disk to a top-hat as the sample surface moves away from the focal plane. As in case of the Gaussian craters, the crater rim height is highest at the focal plane, and decreases with distance

from the focal plane. However, the rim height to crater diameter ratio seems to be constant in the Rayleigh range and starts to decrease beyond it. This implies that the rim height and crater depth decrease at the same rate initially and then the rim height starts decreasing more sharply. ***Thus the top-hat results in a lower rim height to crater depth ratio.***

- **Overall Dependence of Rim Height:** The crater rim height is more a function of the crater dimensions, than of the beam profile. The top-hat beam profile appears to yield a lower rim, but the reduction is small compared to the reduction in rim height achieved by increasing the crater diameter. Hence, craters larger than 30-40 μm are rimless because of their large diameter; while rim heights of craters smaller than approximately 10 μm may be reduced by reshaping the beam into a top-hat.

Table 1: Summary of General Trends as a function of Focal Plane Location

	Gaussian	**Top-Hat**
Crater Width	Smallest at focal plane 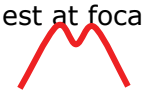	Widest at focal plane 
Crater Depth	Deepest at focal plane 	Deepest at focal plane 
Rim Height	Highest at focal plane 	Highest at focal plane 
Rim Height/Crater Depth	Lowest at focal plane 	Highest at focal plane 

Note: the x-axis for all sketches is 'distance from focal plane', with the focal plane at the center.

5.2 Recommendations for Future Work

The main objective of this project is to understand the reason for the surface roughness observed while making microchannels in dielectric materials using femtosecond laser pulses. Previous studies show that the surface roughness is caused when craters overlap when using multiple laser shots. The rims of the individual craters diffractively interact with each other leading to periodic surface features. The dimension of these microfeatures is of the order of the wavelength of the laser beam.

We have focused entirely on single-shot ablation in this project. The crater profile is expected to mirror the laser pulse spatial profile. Hence the walls of a 'Gaussian' crater should be more slanted than the walls of a 'top-hat' crater. This effect is difficult to identify with single shot ablation craters owing to the small dimensions involved. However, we expect that when multiple pulses overlap at the same spot, the effect would get exaggerated and the walls of craters made with, say, 5 laser pulses, will show drastically different morphology depending on the pulse profile.

The relationship between the crater diameter and the rim height should also be extended to check if the surface roughness decreases when machining large sized multishot ablation channels.

The next logical step is, therefore, to compare the effect of multishot ablation with the Gaussian and the top-hat beam profiles, and with craters or channels of increasing sizes. This should be done both with multishot craters and with continuous channels.

6 Appendix :

6.1 Appendix A: M^2 Measurement

Measuring M^2 factor:

Real-time beam diagnostic measurements are recorded using the UNIQ TM-7CN CCD camera with Spiricon software, having a pixel array of 1254 x 1148 pixels and a pixel size of ~9.8 μm per pixel. A frame grabber card together with Spiricon LBA 300PC software v3.03 is used for the 2-D intensity distribution analysis of the captured digitized images. These measurements are used to determine the lens focal distance, the laser M^2 propagation factor etc.

Detailed specifications on the camera are given at the end of this section.

The following measurements are taken:

- Width of the smallest focused spot in x and y directions
- Position of the focused spot relative to the focal length of the lens
- Beam width at the focal length of lens (might be different from the smallest spot size)
- Divergence angle of the beam beyond focus

Notes:

- The lens is kept fixed and the detector is moved on the rail in the axial direction.
- The measurements were done with two energy calculation settings in the software to validate the calculation
    - 86% energy method
    - Knife-edge method
- The number of 'illuminated pixels' was also counted randomly to check the software calculations.
- Barely enough filters were used so that the CCD chip was just below saturation level, for an accurate beam size measurement.
- Absorbing filters were avoided in the experiment because they have non-linear energy absorption and cause the shape of the beam and hence the divergence and size readings to get distorted. Reflecting filters were used instead.
- Ultracal™ (algorithm provided by Spiricon) was used to eliminate background noise, to ensure better readings.
- Minimum size of the beam should be 100 microns, so that enough signal is received by the CCD chip to ensure correct size calculations
- 'Origin' software was used for the non-linear curve fitting.

Sample Measurements: (Note: this graph is used as an example only)

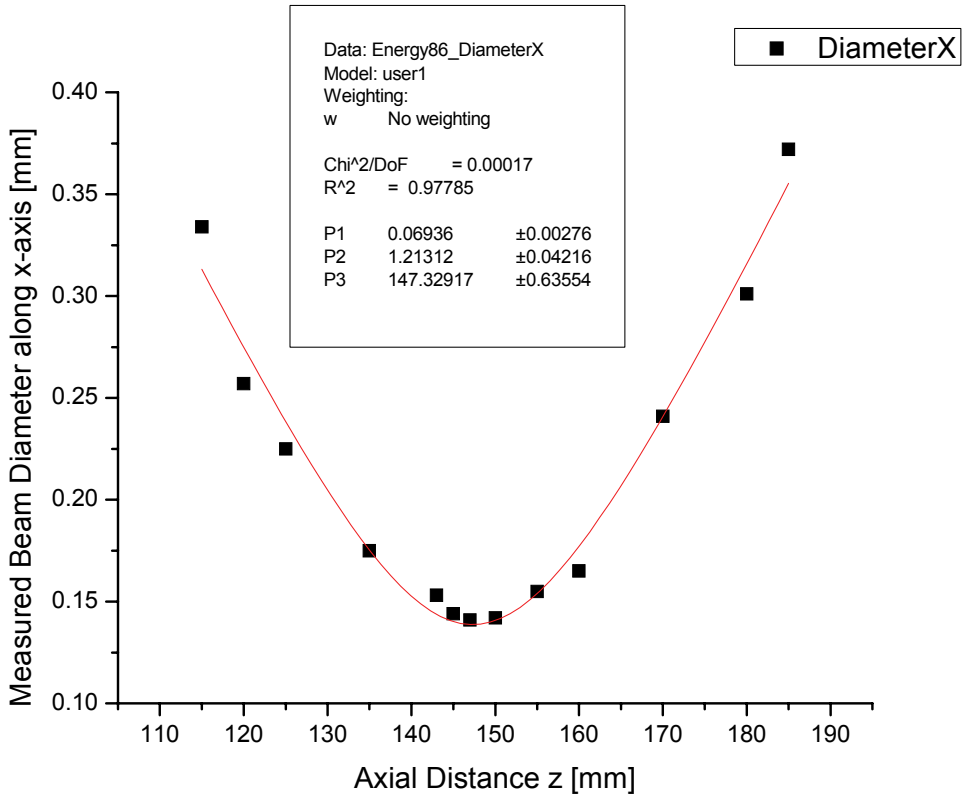

Specifications of the UNIQ CCD (Charge Coupled Device) Camera (model TM-7CN):

Imager	1/2" interline transfer CCD
Sensor Size	6.4(h) x 4.8(v) mm (4:3 Aspect Ratio)
Chip Size	7.95(h) x 6.45(v) mm
Cell Size	8.4(h) x 9.8(v) microns
Pixel Array Size	768H x 494V (Sensor Size/Cell Size)
Output	Analog
Bit Depth	8-bit camera (Grayscale level 256) (Dynamic range 48 dB)
Scanning	525 lines 60Hz
Irising	Auto Iris Lens
Acquisition Rate	30 Hz (interlaced video)
Saturation Level	0.3 $\mu W/cm^2$ CW and 3 nJ/cm^2 pulsed

6.2 Appendix B: Properties of Borosilicate Glass

Properties of borosilicate glass are listed below:

Chemical composition:	81% SiO_2, 13% B_2O_3, 2% Al_2O_3, 4% Na_2O
Band gap energy:	$E_b < 4$ eV
Refractive index:	1.472
Density:	2.23 g/cm3
Abbe Number:	65.7
Coefficient of Linear Expansion:	3.20
Viscosity:	$\approx 10^3$ Pa.s (1500 K) $\approx 10^2$ Pa.s (2000 K) 1-10 Pa.s (>2500 K)
Surface Tension:	0.28 J/m^2
Thermal conductivity:	1.25 W/mK (300 K) 1.60 W/mK (600 K) 4.50 W/mK (900 K) 42.0 W/mK (1500 K)
Specific Heat:	746 $JKg^{-1}K^{-1}$ (300 K) 1000 $JKg^{-1}K^{-1}$ (600 K) 1250 $JKg^{-1}K^{-1}$ (900 K) 1320 $JKg^{-1}K^{-1}$ (1500 K)
Thermal Diffusivity:	0.75 m^2/s (300 K) 0.72 m^2/s (600 K) 1.60 m^2/s (900 K) 14.3 m^2/s (1500 K)
Annealing temperature:	560°C
Softening temperature:	821°C
Working point:	1252°C
Melting Temperature:	1500 K
Strain point:	510°C

6.3 Appendix C: MATLAB Code Listing

```
%CALCULATING VARIATION IN SINGLESHOT ABLATION CRATER DIMENSIONS WITH
DISTANCE FROM FOCAL PLANE
%fluence2
hold on

%Known Parameters from Experiment Setup:
w_0 = 4;  %  initial beam size (radius) in mm
lambda = 0.780e-3;   %wavelength in mm
f = 100; % focal length in mm
F_threshold_single = 2.6;   % J/cm2
F_threshold_multiple = 1.7;   % J/cm2
alpha_inverse = 240; %optical penetration depth in nm
E_pulse = 120e-6;  % incident laser energy in Joules

%Focal Spot Characteristics:
% w_1 = f*lambda/(pi*w_0)   %focal spot size in mm
w_1 = 13.9e-3    %focal spot size [mm], (from spotsize measurements)
z_R = pi * w_1^2/lambda   %Rayleigh range in mm
F_0_peak_0 = (E_pulse*100)/(3.14*w_1^2)  % Peak Fluence Joules/cm^2
D_0  =  (2*w_1^2*log(F_0_peak_0/F_threshold_single))^0.5   %Crater Width
[mm] at Focal Plane
h_0  =  240*log(F_0_peak_0/F_threshold_multiple)    %Crater Depth [nm] at
Focal Plane

%Variation with axial Location:
z = -2:0.1:2;   %axial distance in mm
w_z = w_1*(1+(z./z_R).^2).^0.5;   %beam size at z axial location, in mm
% plot(z/z_R,w_z*1000,'-r')
% title('Fluence'); ylabel('Axial Location z, [mm]');
% hold on
F_0_peak_z = (E_pulse*100)./(3.14*w_z.^2);  %Peak Fluence [Joules/cm^2]
% plot(z/z_R,F_0_peak_z,'.b')
D = (2*w_z.^2.*log(F_0_peak_z./F_threshold_single)).^0.5;  %Crater Size
[mm]
plot(z/z_R,D*1000,'.c')
h_z  =  alpha_inverse*log(F_0_peak_z./F_threshold_multiple);     %Crater
Depth in nm
% plot(z/z_R,h_z,'.r')
% I_0 = 2*P/(pi*w_0^2);
%  I(r,z)  =  I_0*(w_0/w_z)^2*exp(-2*r^2/w_z^2);    Calculation  of  3-D
variation
% of intensity with axial and radial distance

% L = legend('Beam Spot Size [micron]','Fluence [J/cm^2]','Crater Size
% [micron]','Crater Depth/100 [nm]');
% set(L, 'FontSize', 7)
title('Gaussian Beam Profile, f = 100 mm'); xlabel('Distance from Focal
Plane [normalized by Rayleigh range]');
```

6.4 Appendix D: Ablation With Gaussian Beam Profile

Trends Seen with Gaussian Beam Ablation:

1) f = 50 mm, w_0 = 6.2 μm:

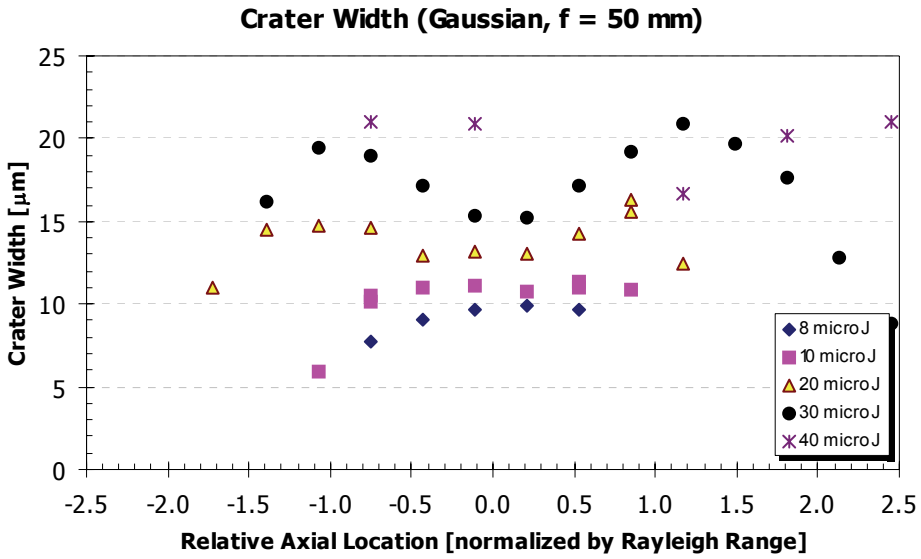

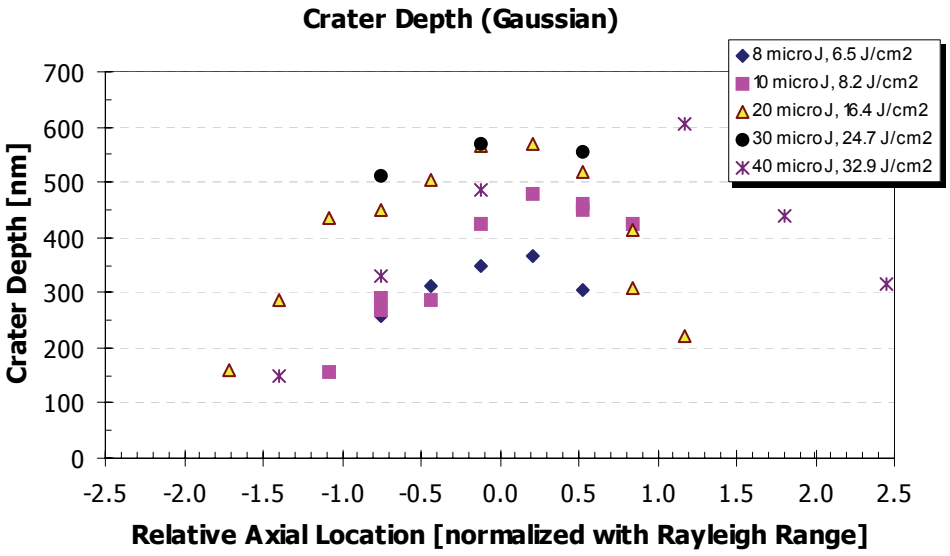

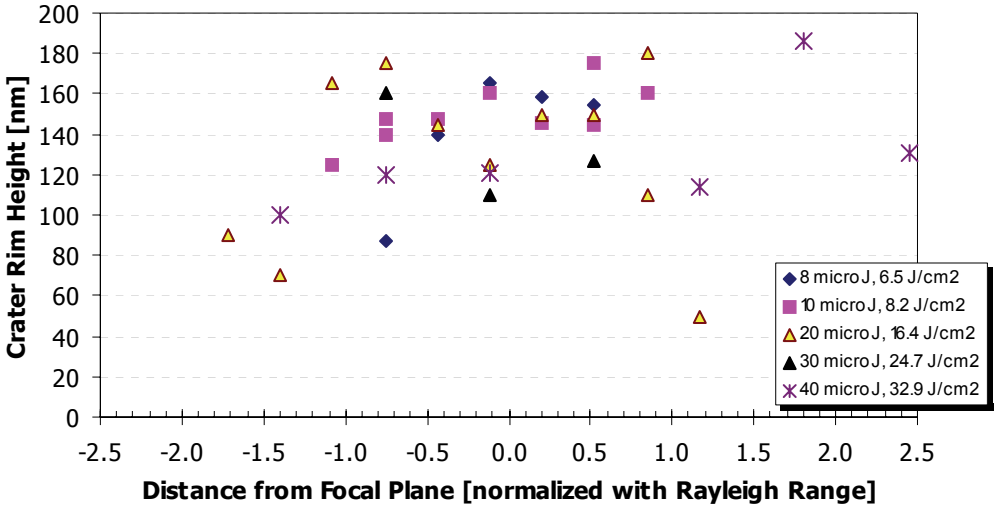
Crater Rim Height [nm]
200
180
160
140
120
100
80
60
40
20
0
-2.5
-2.0
-1.5
-1.0
-0.5
0.0
0.5
1.0
1.5
2.0
2.5
Distance from Focal Plane [normalized with Rayleigh Range]
8 microJ, 6.5 J/cm2
10 microJ, 8.2 J/cm2
20 microJ, 16.4 J/cm2
30 microJ, 24.7 J/cm2
40 microJ, 32.9 J/cm2

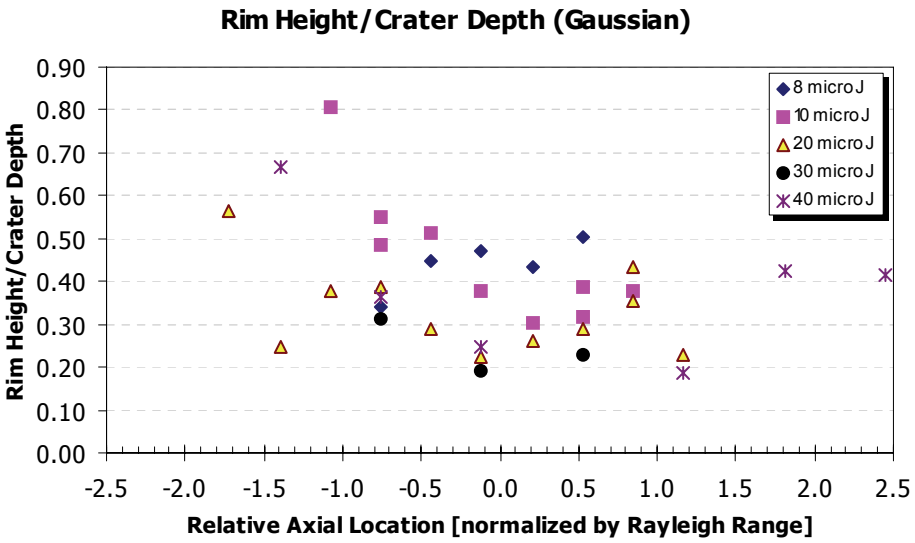
Rim Height/Crater Depth (Gaussian)
Rim Height/Crater Depth
0.90
0.80
0.70
0.60
0.50
0.40
0.30
0.20
0.10
0.00
-2.5
-2.0
-1.5
-1.0
-0.5
0.0
0.5
1.0
1.5
2.0
2.5
Relative Axial Location [normalized by Rayleigh Range]
8 microJ
10 microJ
20 microJ
30 microJ
40 microJ

2) **f = 100 mm, w_0 = 13.9 μm:**

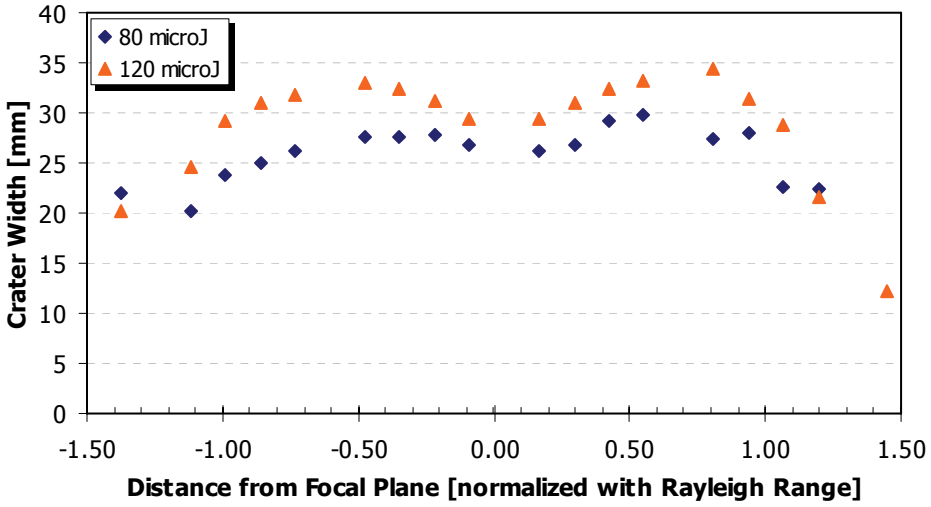

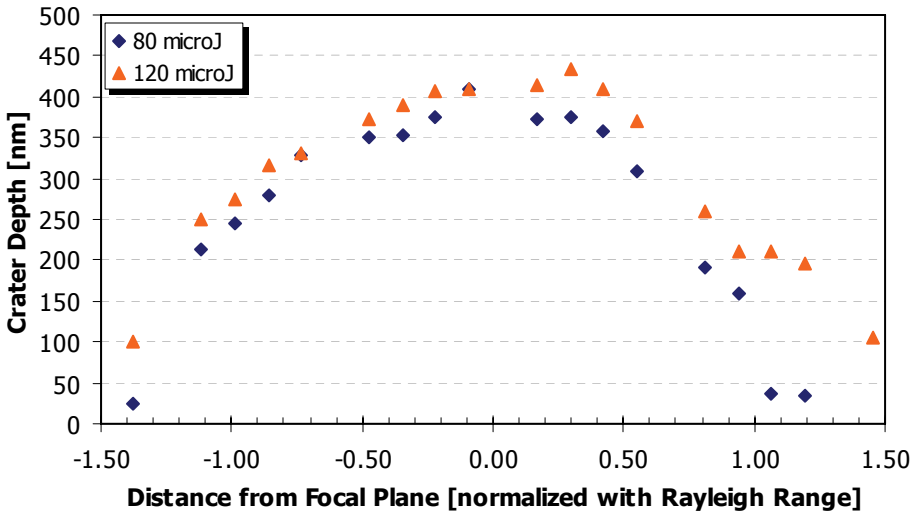

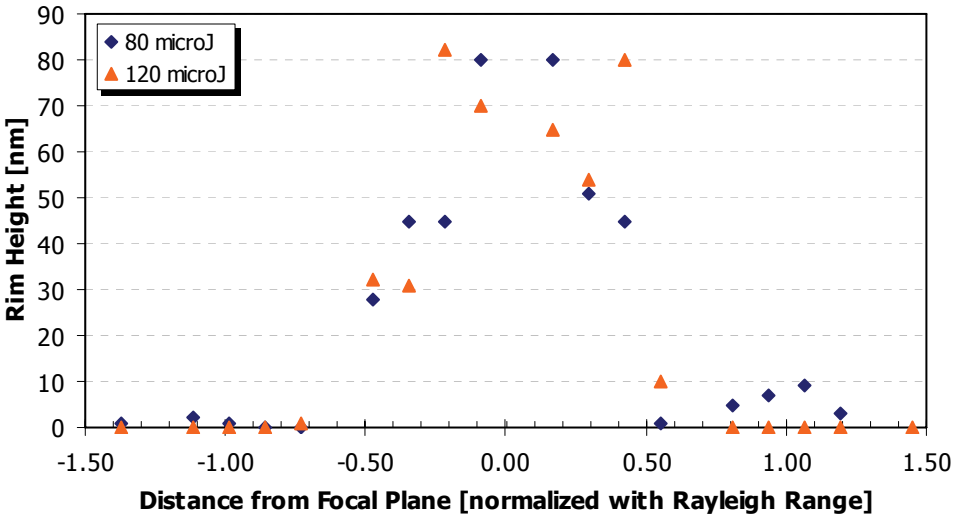

Rim Height/Crater Depth (Gaussian, f=100mm)

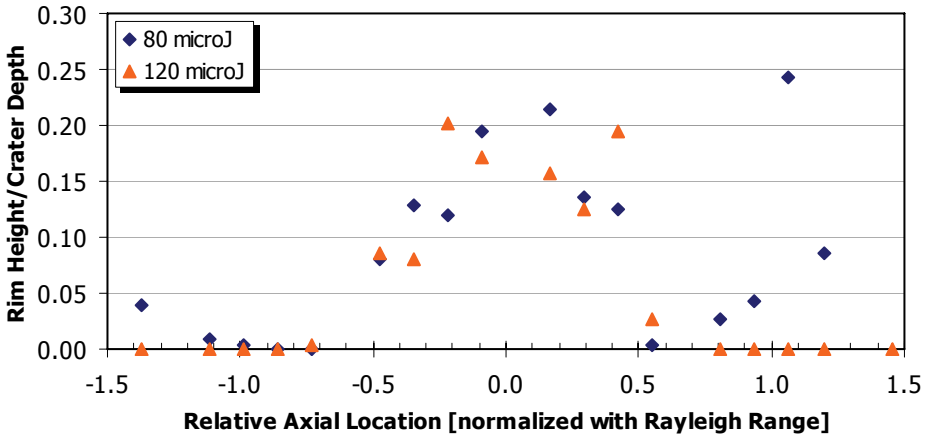

3) f = 250 mm, w_0 = 33.4 μm:

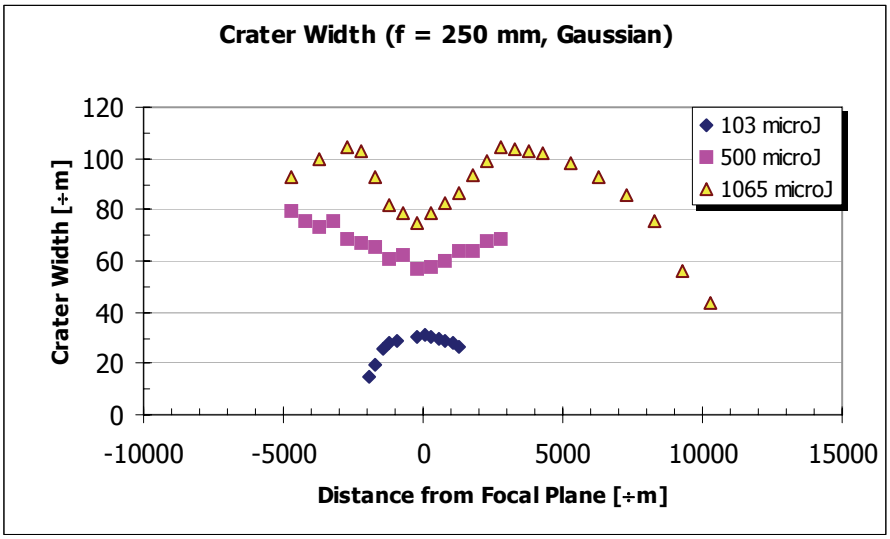

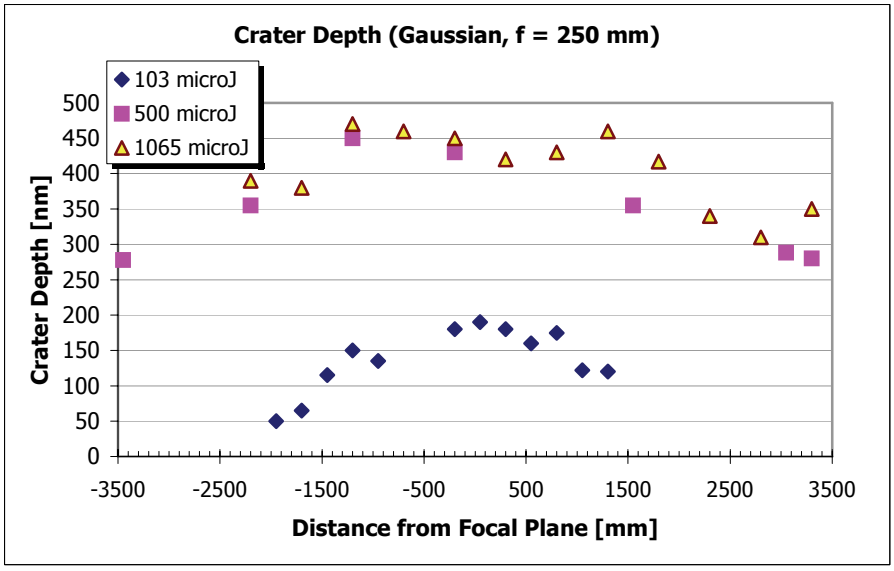

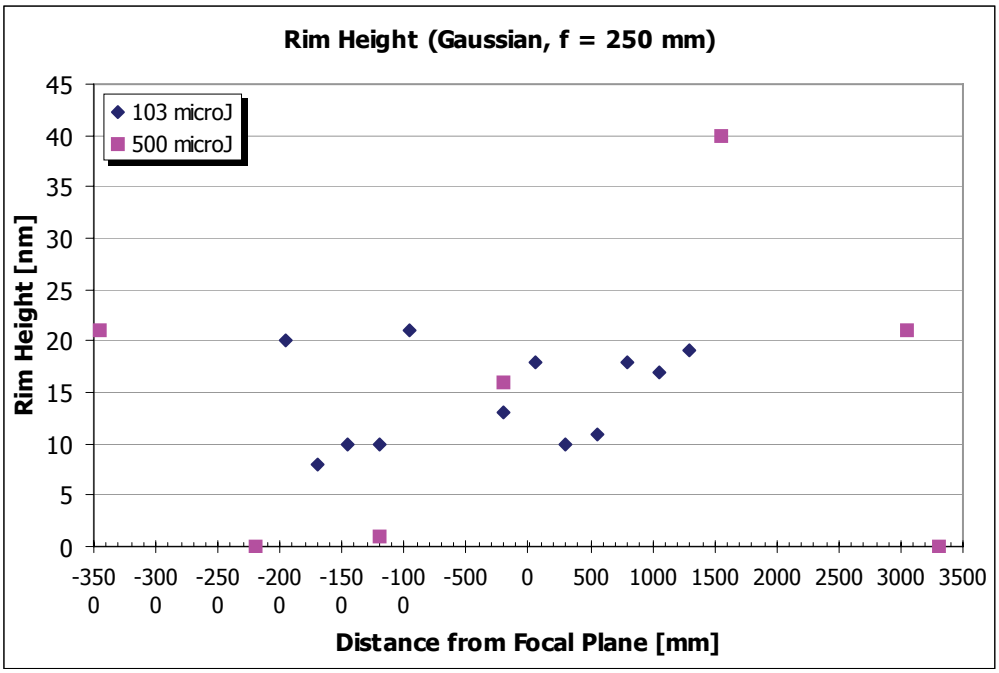
Rim Height (Gaussian, f = 250 mm)
103 microJ
500 microJ
Rim Height [nm]
45
40
35
30
25
20
15
10
5
0
-3500
-3000
-2500
-2000
-1500
-1000
-500
0
500
1000
1500
2000
2500
3000
3500
Distance from Focal Plane [mm]

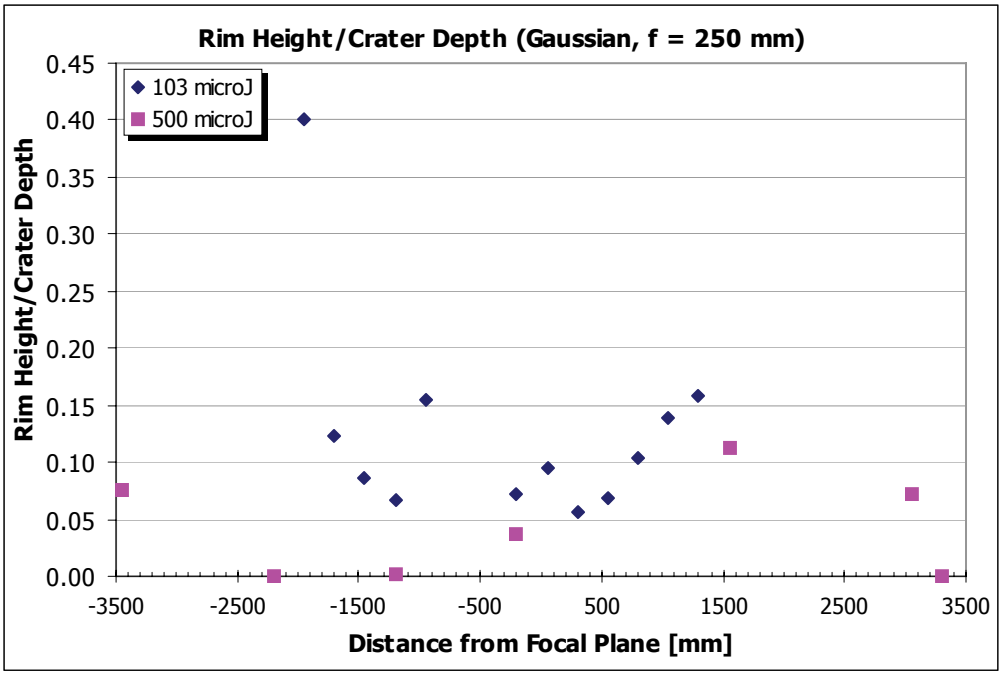
Rim Height/Crater Depth (Gaussian, f = 250 mm)
103 microJ
500 microJ
Rim Height/Crater Depth
0.45
0.40
0.35
0.30
0.25
0.20
0.15
0.10
0.05
0.00
-3500
-2500
-1500
-500
500
1500
2500
3500
Distance from Focal Plane [mm]

6.5 Appendix E: Ablation With Top-Hat Beam Profile

Trends seen with ablation with top-hat beam profile

1) 10X Objective, *NA* = 0.28, w_0 = 4.8 μm:

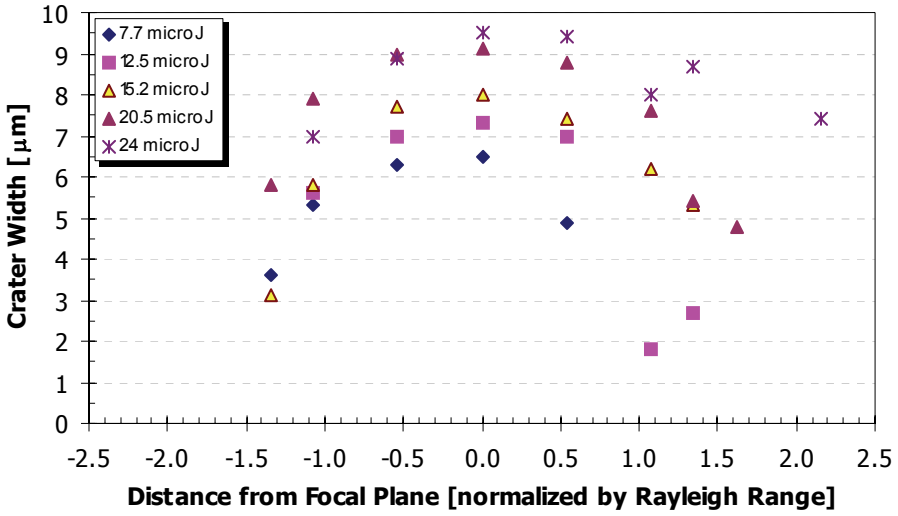

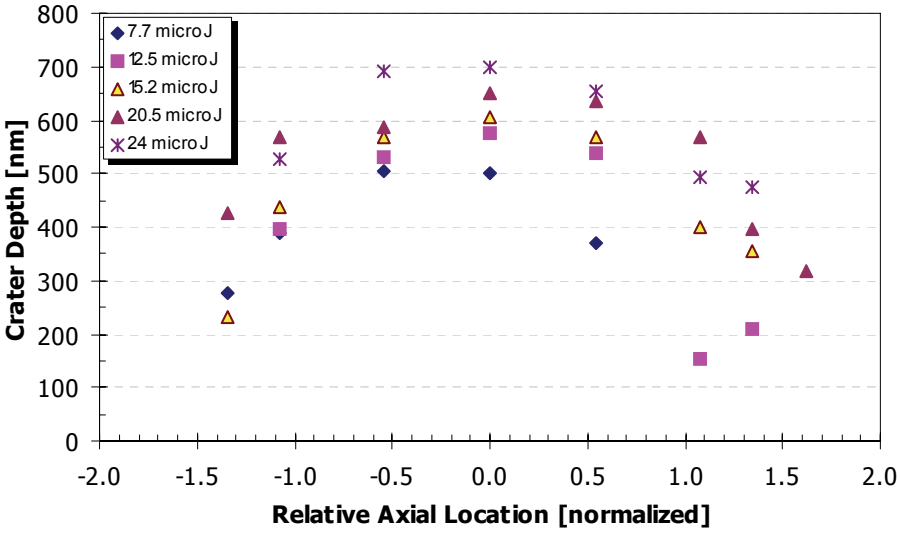

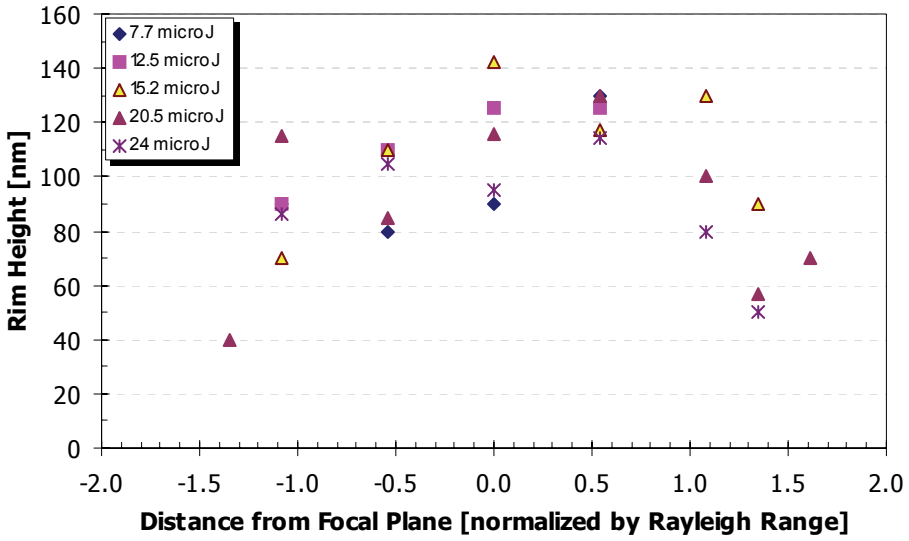
7.7 microJ
12.5 microJ
15.2 microJ
20.5 microJ
24 microJ
Rim Height [nm]
160
140
120
100
80
60
40
20
0
-2.0
-1.5
-1.0
-0.5
0.0
0.5
1.0
1.5
2.0
Distance from Focal Plane [normalized by Rayleigh Range]

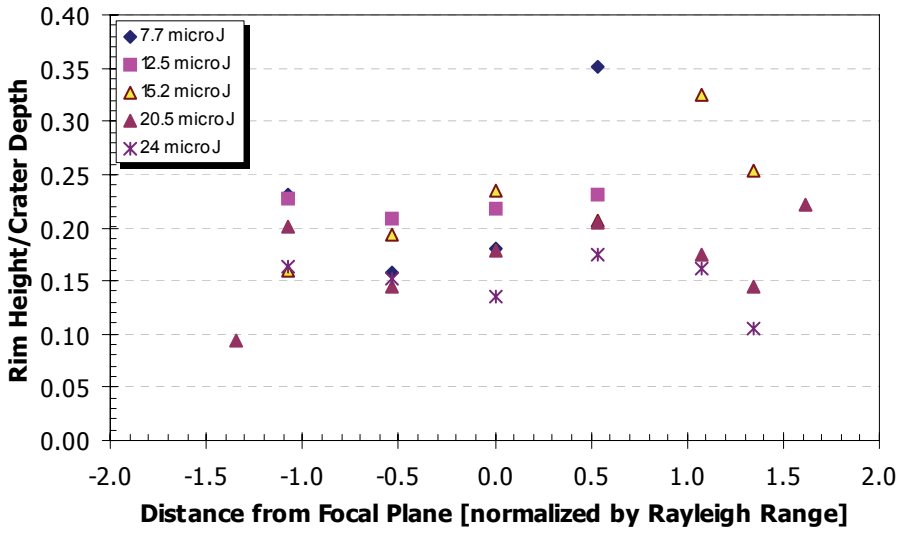
7.7 microJ
12.5 microJ
15.2 microJ
20.5 microJ
24 microJ
Rim Height/Crater Depth
0.40
0.35
0.30
0.25
0.20
0.15
0.10
0.05
0.00
-2.0
-1.5
-1.0
-0.5
0.0
0.5
1.0
1.5
2.0
Distance from Focal Plane [normalized by Rayleigh Range]

2) f = 50 mm, *NA* = 0.06, w_0 = 4.8 μm, E = 50, 80, 296, 409 μJ

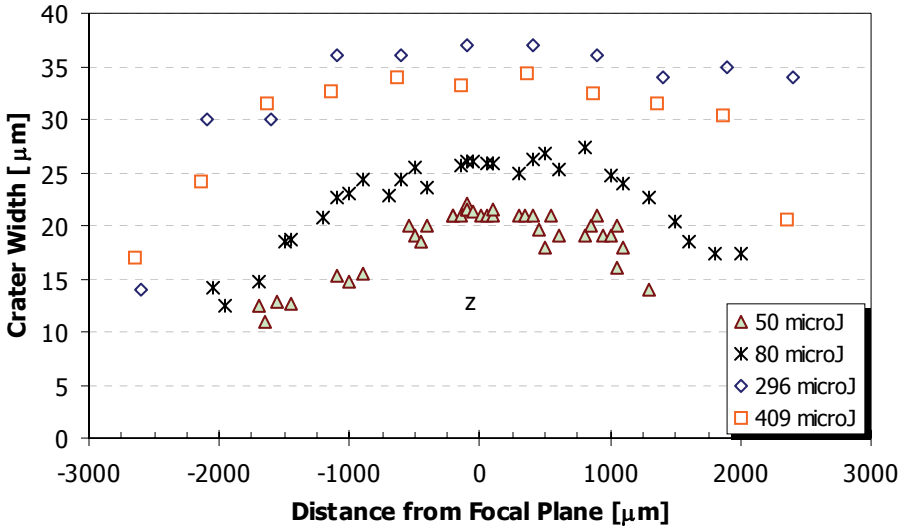

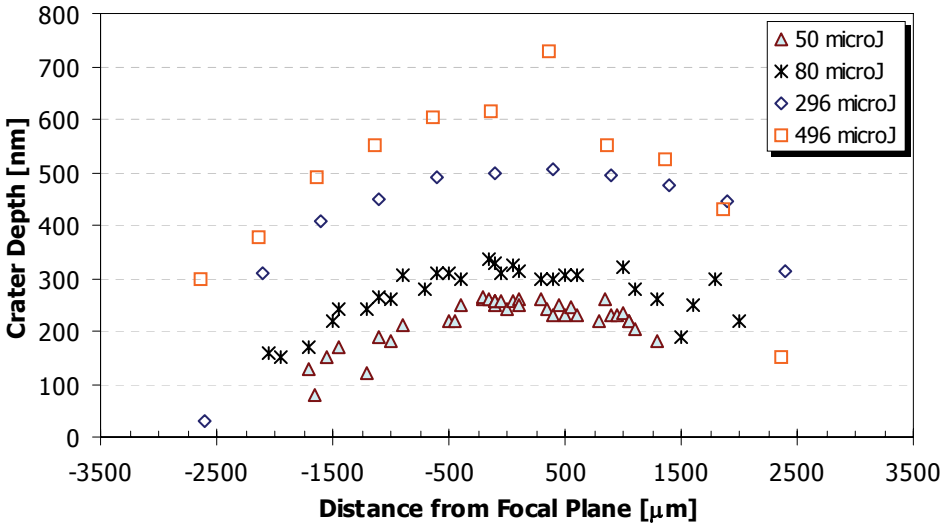

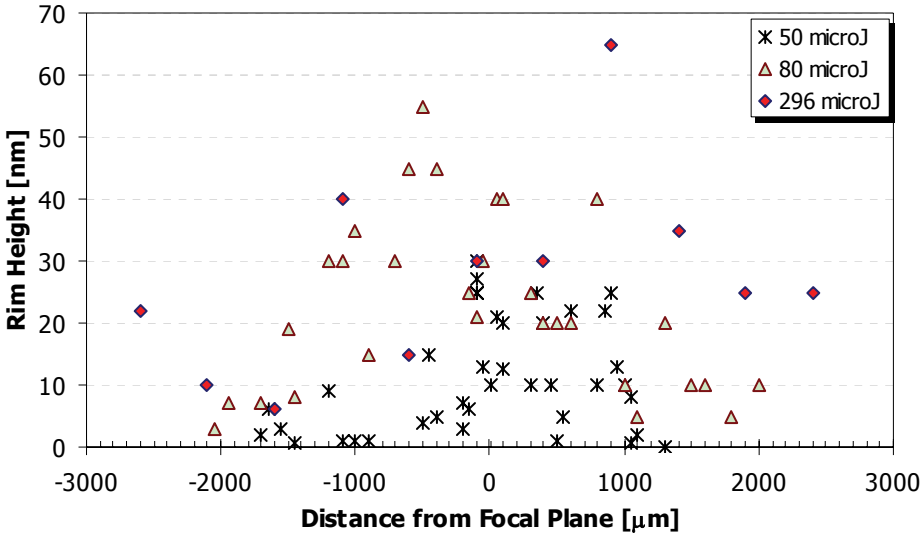
Rim Height [nm]
70
60
50
40
30
20
10
0
-3000
-2000
-1000
0
1000
2000
3000
Distance from Focal Plane [μm]
50 microJ
80 microJ
296 microJ

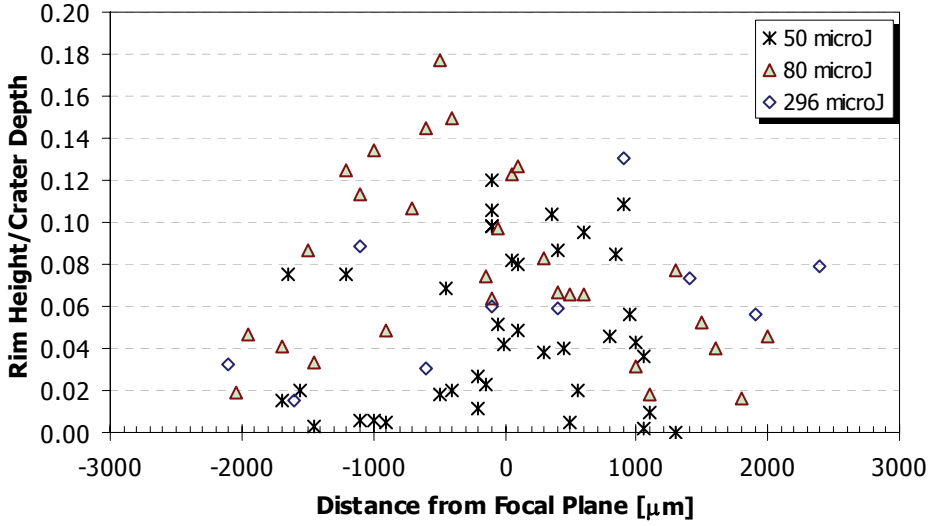
Rim Height/Crater Depth
0.20
0.18
0.16
0.14
0.12
0.10
0.08
0.06
0.04
0.02
0.00
-3000
-2000
-1000
0
1000
2000
3000
Distance from Focal Plane [μm]
50 microJ
80 microJ
296 microJ

7 References:

[1] E. N. Glezer, M. Milosavljevic, L. Huang, R. J. Finlay, T.-H. Her, J. P. Callan, and E. Mazur, *Three-dimensional optical storage inside transparent materials*, Opt. Lett. 21(24) (1996).

[2] A. Marcinkevicius, S. Juodkazis, M. Watanabe, M. Miwa, S. Matsuo, H. Misawa, and J. Nishii, *Femtosecond laser-assisted three-dimensional microfabrication in silica*, Opt. Lett. 26, 277 (2001).

[3] Yan Li, Kazuyoshi Itoh, Wataru Watanabe, Kazuhiro Yamada, and Daisuke Kuroda, *Three-dimensional hole drilling of silica glass from the rear surface with femtosecond laser pulses*, Opt. Lett. 26(23), 1912 (2001).

[4] S. Matsuo, A. Marcinkevicius, R. Waki, K. Yamasaki, M. Watanabe, V. Mizeikis, S. Juodkazis, and H. Misawa, *Three-dimensional modification of transparent materials by focused femtosecond pulses*, Symposium on "Microjoining and Assembly Technology in Electronics" 8th, 489 (2002).

[5] K. Yamasaki, S. Juodkazis, S. Matsuo, H. Misawa, *Three-dimensional micro-channels in polymers: one-step fabrication*, Appl. Phys. A 77(3-4), 371 (2003).

[6] M. Masuda, K. Sugioka, Y. Cheng, N. Aoki, M. Kawachi, K. Shihoyama, K. Toyoda, H. Helvajian, and K. Midorikawa, *3-D microstructuring inside photosensitive glass by femtosecond laser excitation*, Appl. Phys. A 76 857 (2003).

[7] Y. Cheng, K. Sugioka, and K. Midorikawa, *Microfluidic laser embedded in glass by three-dimensional femtosecond laser microprocessing*, Opt. Lett. 29(17), 2007 (2004).

[8] A. Vogel, J. Noack, G. Huttman, and G. Paltauf, *Mechanisms of Femtosecond Laser Nanosurgery of Cells and Tissues*, Appl. Phys. B Invited Paper (2005).

[9] N. Shen, D. Datta, C. B. Schaffe, P. LeDuc, D. E. Ingber, and E. Mazur, *Ablation of Cytoskeletal filaments and Mitochondria in Live Cells using a Femtosecond Laser Nanoscissor*, Mol. & Cell Bio. 2(1), 17 (2005).

[10] I. Maxwell, S. Chung, E. Mazur, *Nanoprocessing of Subcellular Targets using Femtosecond Laser Pulses*, Med. Laser Appl. 20, 193 (2005).

[11] Heisterkamp, I. Z. Maxwell, E. Mazur, J. M. Underwood, J. A. Nickerson, S. Kumar, and D. E. Ingber, *Pulse Energy Dependence of Subcellular Dissection by Femtosecond Laser Pulses*, Opt. Exp. 13(10), 3690 (2005).

[12] M. F. Yanik, H. Cinar, H. N. Cinar, A. D. Chisholm, Y. Jin, and A. Ben-Yakar, *Functional Regeneration After Laser Axotomy*, Nature 432, 822 (2004).

[13] G. Grillon, P. Balcou, J. P. Chambaret, D. Hulin, J. Martino, S. Moustaizis, L. Notebaert, M. Pittman, T. Pussieux, A. Rousse, J. P. Rousseau, S. Sebban, O. Sublemontier, and M. Schmidt, *Deuterium-Deuterium Fusion Dynamics in Low-Density Molecular-Cluster Jets Irradiated by Intense Ultrafast Laser Pulses*, Phys. Rev. Lett. 89(6), 065005 (2002).

[14] T. Baumert, B. Biihler, M. Grosser, R. Tbalweiser, V. Weiss, E. Wiedenmann, and *G.* Cerber, *Femtosecond Time-Resolved Wave Packet Motion in Molecular Multiphoton Ionization and Fragmentation*, J. Phys. Chem. 95, 8103 (1991).

[15] A. Ben-Yakar, R.L. Byer, J. Ashmore, M. Shen, E. Mazur, and H.A. Stone, *Morphology of femtosecond-laser-ablated borosilicate glass surfaces*, Appl. Phys. Lett. 83, 3030 (2003).

[16] C.B. Schaffer, A. Brodeur, and E. Mazur, Laser-induced breakdown and damage in bulk transparent materials induced by tightly focused femtosecond laser pulses, Meas. Sci. and Tech. 12, 1784 (2001).

[17] L.V. Keldysh, Zh. Eksp. Teor. Fiz. 47, 1945 (1964) (Engl. transl. Sov. Phys.–JETP 20, 1307 (1965))

[18] N. Bloembergen, *Laser-induced electric breakdown in solids*, IEEE J. Quantum Electron. 10(3), 375 (1974)

[19] R.W Boyd, *Nonlinear Optics* (Boston: Academic Press, 1992), 1st ed.

[20] M. Gupta, *Handbook of Photonics* (CRC Press 1996).

[21] A.L. Gaeta, *Catastrophic Collapse of Ultrashort Pulses*, Phy. Rev. Lett. 84(16), 3582 (2000).

[22] T. Yau, C. Lee, and J. Wang, Uncollapsed self-focusing of femtosecond pulses in dielectric media due to the saturation of nonlinear refractive index, CLEO (2000).

[23] D. Ashkenasi, G. Müller, A. Rosenfeld, R. Stoian, I.V. Hertel, N.M. Bulgakova, E.E.B. Campbell, *Fundamentals and advantages of ultrafast micro-structuring of transparent materials*, Appl. Phys. A 77, 223 (2003)

[24] M. D. Perry, B.C. Stuart, P.S Banks, M.D. Feit, V. Yanovsky, and A.M Rubenchik, *Ultrashort Pulse Laser Machining of Dielectric Materials*, J Appl Phy 85(9), 6803 (1999).

[25] A. Ben-Yakar, A. Harkin, J. Ashmore, M. Shen, E. Mazur, R.L. Byer, and H.A. Stone, *Thermal and Fluid Process of a Thin Melt Zone during Femtosecond Laser Ablation of* Glass, Proc. SPIE 4977, 335 (2003).

[26] A. Ben-Yakar, and R.L. Byer, Femtosecond Laser Micromachining of Borosilicate Glass for Microfluidic Applications, to be published.

[27] R. Stoian, M. Boyle, A. Thoss, A. Rosenfeld, G. Korn, and I. V. Hertel, and E. E. B. Campbell, *Laser ablation of dielectrics with temporally shaped femtosecond pulses*, Appl. Phy. Lett. 80(3), 353 (2002).

[28] T.D Bennett and L Lei, *Modeling laser texturing of silicate glass*, J Appl Phy 85 (1), 153 (1999)

[29] D. Ashkenasi, A. Rosenfeld, H. Varel, M Wahmer, and E.E.B. Campbell, *Laser Processing of Sapphire with Picosecond and Sub-Picosecond Pulses*, Appl. Surf. Sci. 120, 65 (1997).

[30] T.D Bennett, D.J Krajnovich, L Lei, and D Wan, *Mechanism of topography formation during CO2 laser texturing of silicate glasses*, J Appl Phy 84(5), 2897 (1998).

[31] J. Sun and J. P. Longtin, *Effects of a gas medium on ultrafast laser beam delivery and materials processing*, J. Opt. Soc. Am. B 21(5), 1081 (2004).

[32] A.E. Siegman, *Lasers* (University Science Books, 1986, Chapter 17, 'Physical Properties of Gaussian Beams')

[33] A.E Siegman, *How to (maybe) measure laser beam quality*, OSA TOPS Vol 17, Diode Pumped Solid State Lasers: Applications and Issues, Mark W. Dowley (ed.) (1998)

[34] M.W Sasnett and T.F Johnston, Jr., *Beam Characterization and measurement of propagation attributes*, SPIE Laser Beam diagnostics 1414, 21 (1991)

[35] D.M Karnakis, J Fieret, P.T Rumsby, and M.C Gower, *Microhole drilling using reshaped pulsed Gaussian laser beams*, Exitech Co. Oxford, UK.

[36] J. W. Goodman, *Introduction to Fourier Optics* (McGraw-Hill, New York, 1968).

[37] http://www.oxfordlasers.com/micromachining/pdfs/papertophat.pdf

[38] K. Kanzler, *Transformation of a gaussian laser beam to an Airy pattern for use in focal plane intensity shaping using diffractive optics*, SPIE Con. Laser Beam Shaping II , August 2nd presented in San Diego CA Con # 4443-09.

[39] A. Ben-Yakar, and R.L. Byer, *Femtosecond laser ablation properties of borosilicate glass*, Jour. Appl. Phy. 96, 5316 (2004).

[40] H. T. Yura, and T. S. Rose, *Gaussian Beam Transfer through hard-aperture optics*, Appl. Optics 34(30), 6826 (1995).

8 Vita

Priti Duggal was born in Goslar, W. Germany on February 16, 1980, the elder of two children, to Ashwani Duggal and Mridula Sood. She was home-schooled in Batala (Punjab, India) during the critical high school years. She graduated from the Indian Institute of Technology, (IIT) in Delhi, in August 2001, where she received a Bachelor's degree in Mechanical Engineering. This was followed by a two year work stint with the GE Global Research Center in Bangalore, India, where she developed detailed know-how in the area of gas turbines and information technology. Since August 2003 she has been pursuing her Master of Science degree in Engineering at the University of Texas at Austin.

Permanent Address: 22, Urban Estate,
Batala, Punjab – 143505
India

This thesis was typed by the author.